Energy Conversion and Management 360 (2026) 121588

Contents lists available at ScienceDirect

Energy Conversion and Management

journal homepage: www.elsevier.com/locate/enconman

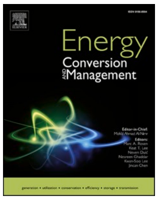

Research Paper

Multiphysics modelling of S3-type flexible tube WECs with distributed DEG PTO: bulge wave dynamics and fluid-structure-electric coupling

Yang Huang [a], Qing Xiao [a,*], Liu Yang [b], Saishuai Dai [a], Saeid Lotfian [a], Feargal Brennan [a]

[a] *Department of Naval Architecture, Ocean & Marine Engineering, University of Strathclyde, Glasgow, UK*
[b] *Advanced Composite Group, Department of Mechanical and Aerospace Engineering, University of Strathclyde, Glasgow, UK*

ARTICLE INFO

Keywords:
Wave energy converter
Flexible tube WEC
Dielectric elastomer generator
Fluid-structure-electric coupling
Distributed power take-off
Multiphysics simulation

ABSTRACT

Flexible tube wave energy converters (WECs) integrated with dielectric elastomer generator (DEG) power take-off systems offer a promising route for adaptive and distributed wave energy harvesting. In this study, a high-fidelity multiphysics fluid–structure–electricity (FSE) modelling framework is developed to investigate the coupled response of an S3 flexible tube WEC with distributed DEG units. The framework combines computational fluid dynamics, nonlinear finite element analysis, and a lumped electromechanical DEG model within a strongly coupled two-way solution strategy. After validation against laboratory measurements of voltage-induced deformation of a dielectric elastomer actuator, the model is used to examine the effects of wave period, wave amplitude, initial voltage, and DEG layer number on structural response and electrical power generation. The results show that electrostatic loading modifies the propagation of bulge waves and the associated deformation modes at short wave periods ($0.9\ \mathrm{s} < T_\mathrm{w} < 1.2\ \mathrm{s}$), whereas at longer wave periods ($1.2\ \mathrm{s} < T_\mathrm{w} < 2.42\ \mathrm{s}$) it primarily amplifies structural deformation. Increasing wave amplitude ratio A_w/D from 0.4 to 0.55 increases the time-averaged electrical power by 27%, accompanied by a 26% rise in the maximum stress. Similarly, increasing the initial voltage V_0 from 1 to 6 kV enhances the mean electrical power by 55 times, while the maximum stress increases by 21%. In addition, the electrical power increases approximately quadratically with number of DEG layer. Overall, the study provides physics-based insights into the coupled FSE mechanisms governing flexible tube WECs and highlights the importance of explicitly resolving electromechanical feedback for reliable performance prediction and design optimisation.

1. Introduction

Wave energy remains an attractive resource for supplying offshore infrastructure and coastal energy systems, yet progress toward practical deployment is still constrained by device cost, survivability, and performance robustness under variable sea states [1–4]. Conventional rigid-body wave energy converters (WECs) typically rely on articulated mechanisms and concentrated power take-off (PTO) units, which may experience high local loads, fatigue accumulation, and sensitivity to off-design conditions [5,6]. In this context, flexible WEC concepts have gained increasing attention because structural compliance can mitigate extreme loading, broaden operational adaptability, and enable new integration routes using soft materials and distributed transduction [7,8]. These characteristics are particularly attractive for wave energy systems aiming to achieve robust and efficient energy conversion under variable and uncertain sea states.

Flexible tube WECs represent a distinct class of flexible devices that harvest wave energy through travelling deformation along a pressurised, submerged tube aligned with the incident wave direction [8]. The wave-induced pressure difference across the tube wall generates propagating bulge waves, producing cyclic cross-sectional expansion and contraction and driving internal pressure dynamics. Energy can be extracted either through conventional hydraulic or turbine-based PTO systems, or via direct electromechanical conversion using dielectric elastomer generators (DEGs).

Two representative concepts based on the bulge wave mechanism are the Anaconda and the S3 [9,10]. In the Anaconda concept, the wave-induced bulge wave energy is transported along the tube and extracted at a single mechanical PTO located at the stern, where the kinetic energy of the internal fluid is first converted into mechanical motion and subsequently into electrical power. By contrast, the S3 concept distributes multiple DEG-based PTO units along the tube length, enabling direct

---

* Corresponding author.
E-mail address: qing.xiao@strath.ac.uk (Q. Xiao).

https://doi.org/10.1016/j.enconman.2026.121588
Received 13 January 2026; Received in revised form 5 April 2026; Accepted 3 May 2026

conversion of local structural deformation into electrical output without intermediate mechanical transmission stages.

This distributed PTO architecture is a key feature of S3-type WECs. As illustrated in Fig. 1, multilayer dielectric elastomer (DE) membranes are embedded within the flexible tube wall and operate in conjunction with a control circuit. As bulge waves propagate along the tube, local cross-sectional contraction activates the DEG units and generates electrical energy. Compared with flexible oscillating water column (OWC) WECs employing a single DEG unit as the PTO, the S3-type distributed PTO system enables energy harvesting along the entire deforming structure, avoids concentrating power extraction and structural loads at a single location, and thereby enhances operational robustness, power continuity, and scalability of the energy conversion process.

Despite these conceptual advantages, the practical implementation of DEG-integrated flexible tube WECs in energetic marine environments remains challenging. Issues such as material durability, long-term reliability, and survivability under highly variable wave loading still require further investigation before such concepts can be considered for practical deployment. At the same time, accurately predicting the dynamic response of S3-type WECs is also highly challenging. The system involves strongly coupled interactions among the external wave field, internal fluid motion within the tube, deformation of a slender and flexible structure, and electromechanical coupling induced by the embedded DEG-based PTO system. The coexistence of internal and external flows, together with distributed deformation and spatially varying electrical actuation, leads to a highly nonlinear multiphysics response that cannot be reliably captured using simplified or decoupled modelling approaches.

Existing experimental and numerical studies have clarified key hydroelastic features such as resonance behaviour, bulge wave propagation, and the influence of PTO impedance [8,11–15]. However, most numerical approaches rely on reduced-order descriptions, including potential-flow hydrodynamics combined with linearised wall dynamics or simplified representations of internal flow [11,15]. While computationally efficient, these models are generally not intended to resolve nonlinear free-surface effects during intermittent tube emergence, internal flow redistribution within a strongly deforming tube, or spatially resolved stress distributions along the structure, which are critical for design evaluation and durability assessment. More importantly for DEG-enabled concepts, PTO effects are often represented through equivalent damping or impedance models, such that the feedback of electric-field-induced pressure on deformation, stress response, and hydroelastic behaviour is not explicitly captured.

High-fidelity computational fluid dynamics (CFD)-finite element analysis (FEA) frameworks offer a route to address these limitations and have been increasingly adopted for flexible structure-wave interaction problems [16–21]. Nevertheless, extending such approaches to DEG-enabled flexible tube WECs is non-trivial because the electrical subsystem is not a passive load: the electric-field-induced pressure depends on the instantaneous geometry (e.g., membrane thickness and electrode separation), while the resulting electromechanical loading alters deformation, stress, and ultimately power output. This bidirectional coupling creates a fluid–structure-electricity (FSE) interaction that must be resolved consistently to obtain physically reliable predictions and to support design and control optimisation.

Building on a previously validated CFD-FEA framework developed for flexible WEC hydrodynamics [21,22], the present work incorporates a capacitor-based DEG description to account for electric-field-induced loading and power generation, thereby establishing a strongly coupled FSE modelling capability. The underlying fluid–structure interaction (FSI) basis has been validated in our previous studies, while the newly introduced electromechanical extension is further assessed here against laboratory measurements of voltage-induced deformation of a dielectric elastomer (DE) actuator under controlled electrical loading. It should be noted that the present study is intended to develop a high-fidelity multiphysics framework for mechanism analysis and design-oriented assessment of DEG-integrated flexible tube WECs, rather than to claim full experimental validation of the complete S3 system under dynamic wave conditions. On this validated basis, the framework is applied to the S3 flexible tube WEC to quantify how wave conditions and electrical parameters, including the initial voltage and number of DEG layers, govern deformation modes, stress response, and spatially distributed power generation. The results provide physics-based insights into when electric-field-induced pressure modifies bulge wave dynamics and when it primarily amplifies deformation, while also clarifying the associated trade-off between enhanced mean power output and increased amplitude of power variation.

The remainder of this paper is organised as follows. Section 2 introduces the multiphysics formulation and coupling strategy. Section 3 presents validation cases. Section 4 describes the S3 model setup, PTO system, and simulation matrix. Section 5 discusses the coupled responses and power generation characteristics under varying wave and electrical conditions. Section 6 summarises the conclusions and outlines future work.

2. Multiphysics modelling framework

In our previous studies, a coupled fluid–structure interaction (FSI) framework integrating CFD and FEA was developed to simulate complex FSI problems [22]. The framework has been systematically validated against a range of benchmark cases, demonstrating its accuracy and numerical robustness. It has subsequently been applied to the investigation of wave-induced dynamic responses of flexible oscillating water column (OWC) WECs and flexible tube WECs [19,20].

Building upon this established FSI framework, an electrostatic field solver has recently been incorporated to account for electromechanical coupling effects. The resulting fluid–structure-electricity (FSE) framework enables a comprehensive multiphysics description of the coupled hydrodynamic, structural, and electrical behaviours of DEG-integrated flexible WECs. This enhanced framework has been successfully employed to analyse a novel flexible WEC concept that combines OWC technology with DEG-based power take-off (PTO) systems [21].

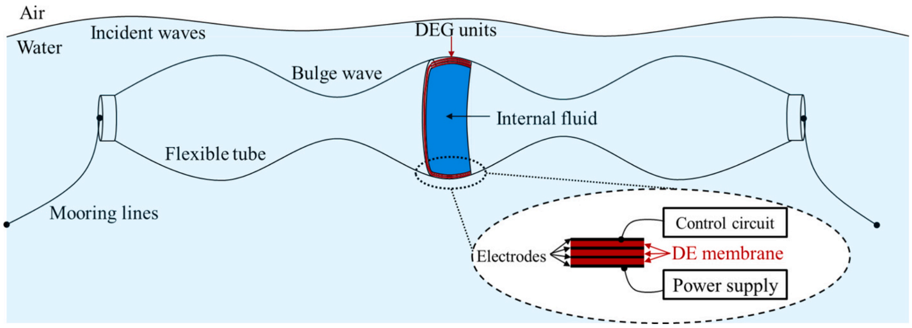

Fig. 1. Schematic of S3-type flexible tube WECs with distributed DEG PTOs.

In the present study, the developed FSE framework is adopted to investigate the coupled multiphysics response of a flexible tube WEC equipped with DEG-based PTO systems. A concise description of the numerical framework and coupling strategy is provided in the following subsection.

2.1. Hydrodynamic modelling

To accurately resolve the transient viscous flow both inside and outside the flexible tube wave energy converter, large-eddy simulation (LES) is adopted. The fluid motion is governed by the three-dimensional (3D) incompressible Navier-Stokes equations, which can be written as

$$\frac{\partial \overline{u}_i}{\partial x_i} = 0, \tag{1}$$

$$\frac{\partial \rho \overline{u}_i}{\partial t} + \frac{\partial}{\partial x_j}\left[\rho \overline{u}_i\left(\overline{u}_j - \widehat{u}_j\right)\right] = -\frac{\partial \overline{p}_i}{\partial x_i} + \frac{\partial}{\partial x_j}\left[\mu_e\left(\frac{\partial \overline{u}_i}{\partial x_j} + \frac{\partial \overline{u}_j}{\partial x_i}\right)\right] - \frac{\partial \tau_{ij}}{\partial x_j} + \rho g_i + f_\sigma, \tag{2}$$

where x_i denotes the Cartesian coordinates in the x, y, and z directions, and $\overline{u}_i$ represents the resolved filtered velocity component. The fluid density is denoted by ρ, and $\overline{p}_i$ is the resolved filtered pressure. The mesh velocity is represented by $\widehat{u}_j$, accounting for grid motion induced by structural deformation. The effective dynamic viscosity is defined as $\mu_e = \rho(\nu + \nu_t)$, where ν and ν_t are the kinematic and eddy viscosities, respectively. The terms g_i and f_σ correspond to gravity acceleration and surface tension force.

The subgrid-scale (SGS) stress tensor, defined as $\tau_{ij} = \overline{u_i u_j} - \overline{u}_i \overline{u}_j$, is modelled using the standard Smagorinsky model [23]:

$$\tau_{ij} = -2\upsilon_S \overline{S}_{ij}, \tag{3}$$

$$\upsilon_S = (C_s\Delta)^2\left(2\overline{S}_{ij}\overline{S}_{ij}\right)^{1/2}, \overline{S}_{ij} = \frac{1}{2}\left(\frac{\partial \overline{u}_i}{\partial x_j} + \frac{\partial \overline{u}_j}{\partial x_i}\right), \tag{4}$$

where υ_S is the SGS eddy viscosity and $\Delta = (\Delta x \Delta y \Delta z)^{1/3}$ denotes the local spatial filter width determined by the resolution. The Smagorinsky coefficient C_s is set to 0.14, consistent with previous numerical studies of free surface and coastal flows [24,25].

The fluid domain is discretised using the finite volume method (FVM). The volume-of-fluid (VOF) approach is employed to capture the evolution of the air–water interface. Pressure-velocity coupling is handled using the PIMPLE algorithm in OpenFOAM, which combines the advantages of the PISO and SIMPLE schemes to achieve stable and efficient time integration for unsteady flows involving moving meshes. Temporal discretization is performed using a second-order Crank-Nicolson scheme, while convective terms are discretised with a second-order upwind scheme. Spatial gradients are evaluated using a second-order limited Gauss linear scheme to maintain a balance between numerical accuracy and stability.

Both air and water are treated as incompressible fluids in the present simulations. This assumption is justified by the relatively low flow velocities of the air phase, for which density variations are negligible. Similar incompressible formulations have been successfully adopted in previous numerical investigations of flexible wave energy converters [19,20].

2.2. Structural modelling

The structural deformation of the flexible tube is governed by the conservation of linear momentum. Based on Newton's second law, the governing equation can be expressed as

$$\rho_s \frac{\partial^2 \mathbf{U_s}}{\partial t^2} = \nabla \cdot \boldsymbol{\sigma} + \mathbf{f}, \tag{5}$$

where $\mathbf{U_s}$ denotes the displacement vector, ρ_s is the material density, $\boldsymbol{\sigma}$ represents the Cauchy stress tensor, and $\mathbf{f}$ is the body forces per unit volume.

The structural governing equations are discretised in space using a 3D finite element method (FEM). Geometric nonlinearities are retained to account for deformation-induced changes in the structural configuration during fluid–structure interactions. Temporal integration is carried out using the implicit Newmark-β method [26], which provides stable time integration for the transient structural response under hydrodynamic loading.

In the present study, the flexible tube is represented using a linear elastic constitutive model. This assumption is adopted for the current simulations and does not represent an intrinsic limitation of the proposed FSE framework, within which more advanced constitutive descriptions, including hyperelastic material models, can be incorporated where required.

2.3. Electromechanical modelling

The DEG-based PTO system consists of multiple layers of DE membranes integrated with an external control circuit. Each membrane is coated on both surfaces with compliant and flexible electrodes. Through a stacked configuration, these membranes collectively form the load-bearing body of the flexible tube. From an electrical perspective, the DEG assembly can be idealised as a set of compliant, deformable parallel-plate capacitors connected in parallel.

During operation, an externally applied voltage generates an electrostatic pressure on the DEG membranes, which in turn affects the mechanical deformation of the tube. Conversely, membrane stretching modifies the electrode area and membrane thickness, thereby altering the capacitance and electrical response. As a result, a bidirectional electromechanical coupling is established between the structural and electrical subsystems, enabling direct conversion of mechanical deformation into electrical output.

In the present study, the electrical behaviour is not resolved as a fully distributed 3D electrostatic field problem. Instead, each distributed DEG unit is represented by a lumped electromechanical submodel associated with its corresponding membrane region. For each unit, deformation-related quantities obtained from the structural solution, including the effective stretch, electrode area change, and thickness variation, are used to update the instantaneous capacitance and electrostatic response. The resulting electrostatic pressure is then applied back to the same membrane region as an equivalent distributed structural load. In this way, the electromechanical coupling is introduced at the DEG unit scale while remaining fully linked to the 3D structural deformation of the tube.

Under a quasi-static electrostatic assumption, the electrostatic pressure (p_e) acting on the membrane is derived from the Maxwell stress tensor. For the parallel-plate capacitor configuration, the electrostatic pressure acting normal to the membrane surface can be expressed as [27]

$$p_\mathrm{e} = \frac{n^2 \varepsilon_0 \varepsilon_\mathrm{r} V^2}{2{t_\mathrm{m}}^2}, \tag{6}$$

where ε_0 is the vacuum permittivity, ε_r denotes the relative permittivity of the dielectric elastomer, and n is the number of stacked membrane layers. The applied voltage V represents the instantaneous voltage across the DE membranes and varies with time, while t_m represents the instantaneous total thickness of all stacked membranes and evolves dynamically with structural deformation.

It should be noted that the above expression for electrostatic pressure is valid under the assumption that the membrane thickness is much smaller than the characteristic diameter (D) of the flexible tube, i.e. $t_\mathrm{m} \ll D$. This condition is satisfied for the geometric configurations considered in the present study. Additionally, the quasi-static electrostatic assumption is adopted for the present electromechanical submodel only and does not constitute an intrinsic limitation of the overall fluid–structure-electricity coupling framework. The proposed framework is modular in nature, and more advanced electrical submodels may be incorporated into the same framework in future work if required.

2.4. *Fluid-structure-electricity coupling strategy*

The coupled multiphysics framework employed in this study combines three specialised solvers to resolve the fluid, structural, and electrical subproblems. The incompressible two-phase flow is solved using OpenFOAM [28], while the structural dynamics of the flexible tube are handled by CalculiX [29]. The electromechanical interaction of each distributed DEG unit is represented using a lumped deformable parallel-plate capacitor model. Information exchange and synchronisation among the different physical domains are managed through the open-source coupling library preCICE [30]. In the present partitioned framework, the structural field serves as the intermediary interface between the 3D fluid domains and the lumped electromechanical model.

A strongly coupled, two-way interaction strategy is adopted to capture the mutual dependence among the internal fluid, external fluid, structural deformation, and electrical response, as schematically illustrated in Fig. 2. At each coupling step, hydrodynamic pressures from the internal and external flow fields are transferred to the structural solver as distributed surface loads acting on the tube wall. Based on the updated structural solution, the deformation state of each membrane region associated with a DEG unit is extracted, including the effective stretch, area change, and thickness variation. These quantities are passed to the electromechanical model to update the capacitance and compute the corresponding electrostatic pressure. The resulting electrostatic pressure is then applied back to the same structural region as an equivalent distributed load. Therefore, the electrical response is coupled to the fluid field indirectly through the structural deformation.

To accommodate the use of independent solvers and numerical formulations for each physical field, a partitioned coupling approach is employed [30]. Strong coupling is enforced through iterative subiterations within each physical time step, ensuring consistent equilibrium among the transferred loads, structural displacements, and electromechanical response across the coupled domains. An implicit time integration strategy is adopted, which allows for stable simulations using relatively large time steps while maintaining numerical robustness in the presence of strong multiphysics interactions.

Data transfer between the non-matching fluid and structural meshes is performed using radial basis function interpolation [31]. In this process, hydrodynamic loads are mapped from the fluid domains onto the structural mesh, while structural displacements are communicated back to the fluid domains to update the moving boundaries. For the electromechanical coupling, deformation-related quantities are extracted from the corresponding structural membrane regions and passed to the DEG submodel, and the computed electrostatic pressures are then applied back to those regions as equivalent distributed structural loads. Convergence of the coupled system is assessed by monitoring the discrete l_2-norm of the solution difference between successive coupling iterations. A time step is considered converged when the prescribed tolerance is satisfied or when a predefined maximum number of coupling iterations is reached, after which the simulation advances to the next time step.

3. Model validation and scope of validation

The FSI component of the proposed framework is built upon our previously developed high-fidelity CFD-FEA model for flexible tube WECs, which has been extensively validated in earlier studies [22]. In those studies, the hydroelastic responses of flexible tube, including the coupled fluid and structural dynamics, were assessed against available experimental data and benchmark cases. Building on this validated FSI basis, the present work introduces an additional electromechanical coupling module to establish the FSE formulation.

Accordingly, the validation effort in the present study focuses on the newly introduced electromechanical component. To this end, numerical predictions are compared against independent experimental measurements reported in the literature [32]. The selected experiment investigates voltage-induced axial deformation of a cylindrical DE actuator under controlled electrical loading, providing a suitable benchmark for evaluating the accuracy of the DEG-based electromechanical model employed here.

It should be noted that this validation strategy is intended to assess the newly added electromechanical extension on top of an already validated FSI basis, rather than to claim full experimental validation of the integrated S3 FSE system under dynamic wave conditions. Dedicated wave tank validation of the fully coupled response, including bulge wave dynamics, internal flow redistribution, resonance characteristics, and electrical power output, remains an important task for future work.

3.1. *Description of the experimental configuration and numerical model*

As illustrated in Fig. 3, the reference experiment considers a cylindrical dielectric elastomer actuator coated with compliant electrodes and subjected to step-wise high-voltage excitation. The actuator consists of a silicone elastomer tube with carbon grease electrodes applied to its inner and outer surfaces. Under electrical loading, electrostatic pressures generated by the applied voltage induce axial deformation of the actuator. The key geometric, mechanical, and electrical parameters of the cylindrical actuator are summarised in Table 1.

To reproduce the experimental conditions, the numerical model adopts the same geometric configuration and material properties as

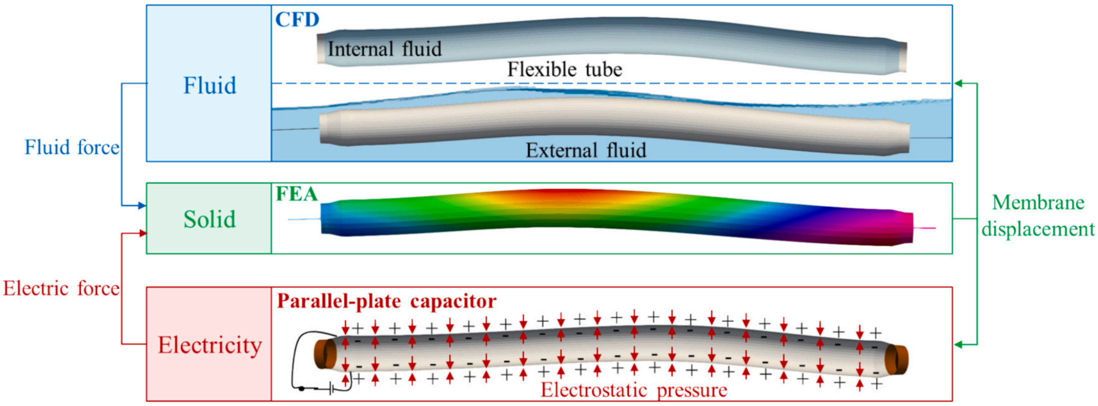

Fig. 2. Schematic of the two-way coupled fluid–structure-electricity modelling framework for the flexible tube WEC.

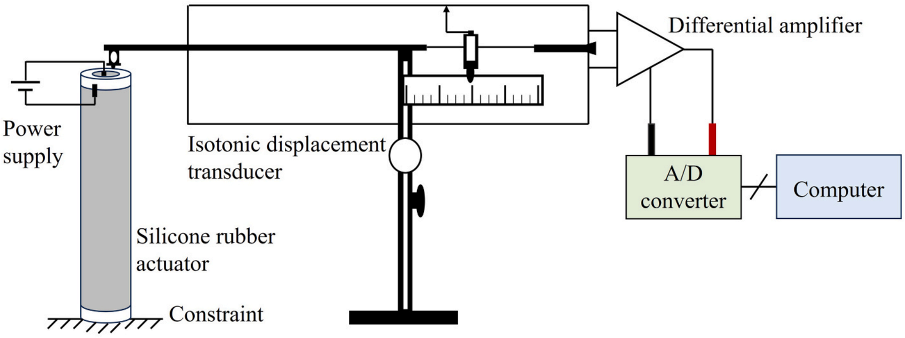

Fig. 3. Schematic of the experimental setup for the electrically activated cylindrical DE actuator.

Table 1
Key parameters of the electrically activated cylindrical actuator.

Material	Silicone (01502 type)
Young's modulus	5 MPa
Permittivity	$3.0 \times 8.85 \times 10^{-12}$ Fm^{-1}
Axial length	50 mm
External diameter	2 mm
Wall thickness	0.2 mm
Axial pre-strain	5%

those reported in the experiment. The dielectric elastomer is modelled as a linear elastic solid, consistent with the small-strain assumption employed in the experimental study. Electrostatic pressures are calculated using the parallel-plate capacitor formulation and applied to the structural model as distributed surface loads. The electrical loading history is prescribed to match the step-wise voltage excitation used in the experiment.

3.2. *Comparison between numerical predictions and experimental measurements*

Fig. 4 compares the numerically predicted axial strain with the experimental measurements under step-wise voltage excitation. The numerical model successfully captures both the trend and magnitude of the axial deformation observed in the experiment. In particular, the predicted peak axial strain shows good agreement with the measured value of approximately 1.2% at a voltage per unit wall thickness of 50 V/μm.

The observed agreement demonstrates that the proposed electromechanical formulation is capable of accurately describing voltage-induced deformation of dielectric elastomer structures within the considered deformation range. This validation provides confidence in the applicability of the FSE framework for analysing DEG-integrated flexible WECs, in which similar electromechanical coupling mechanisms govern the energy conversion process.

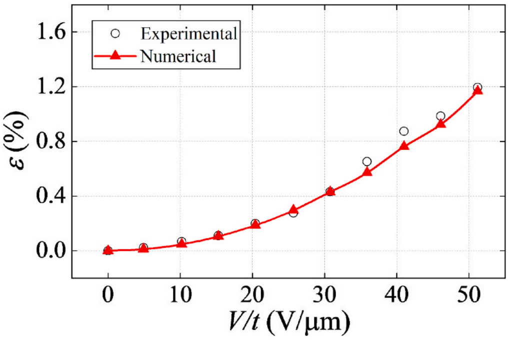

Fig. 4. Comparison between experimental measurements and numerical predictions of axial strain as a function of applied voltage per unit wall thickness for the cylindrical DE actuator.

4. Numerical model configuration and simulation conditions

4.1. *Configuration of the S3 WEC*

In this study, an S3-type flexible tube WEC is investigated. The overall device configuration is based on the concepts proposed by Jean et al. [10] and Babarit et al. [15]. To improve numerical robustness while preserving the essential dynamic characteristics of the system, a shorter flexible tube is adopted in the present simulations. A linear elastic material model is also employed for the flexible tube, using material parameters consistent with those adopted in previous experimental and numerical studies of the S3 WEC [10,15].

As illustrated in Fig. 5, the S3 WEC is positioned close to the free surface, with the top of the flexible tube located 0.15 m below the mean water level. The device consists of rigid bow and stern sections connected by a flexible tube. The bow and stern sections each have a length of 0.1 m, while the flexible tube has a length $L = 3.5$ m. Both the rigid sections and the flexible tube share an external diameter of $D = 0.2$ m.

The flexible tube is made of natural rubber. For the deformation range considered in this study, its mechanical behaviour is represented using a linear elastic constitutive model, with a Young's modulus of 0.75 MPa and a density of 960 kg $\bullet$ m^{-3}. Both ends of the tube are sealed and internally pressurised with water, resulting in an initial pre-stretch of the membrane. The internal pressure is set to 8.2 kPa.

The S3 WEC is anchored at both ends using two mooring lines, allowing the device to undergo six-degree-of-freedom (6DoF) motion in response to incident waves. In the numerical model, the mooring lines are represented by linear springs to capture their primary restoring behaviour. The moorings are symmetrically arranged along the x-axis, with a stiffness of 100 N $\bullet$ m^{-1} and an initial pretension of 57.7 N.

4.2. *DEG-based PTO system*

The operating principle of the DEG-based PTO system is to convert elastic potential energy stored in the deformed DEG membranes into electrical energy. Specifically, when the deformation of a DEG membrane decreases, its thickness increases, and electrical work is performed against the electrostatic forces acting on the membrane surface. This electromechanical energy conversion process requires an external control circuit together with an appropriate control strategy.

An external control circuit is employed to enable electromechanical energy conversion in the DEG-based PTO, following established harvesting strategies reported in the literature [33]. As illustrated in Fig. 6 (a), the control circuit governs the charging, energy extraction, and discharging stages of the DEG during cyclic deformation. In the numerical model, the deformable DEG membrane is represented as a capacitance that varies dynamically with structural deformation. This

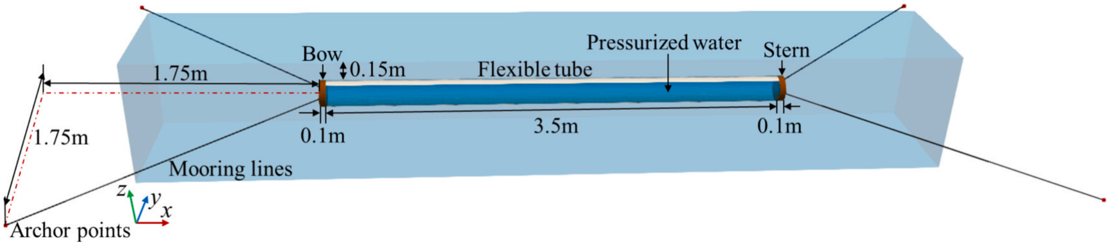

Fig. 5. Schematic of the S3 WEC and configuration of the mooring lines.

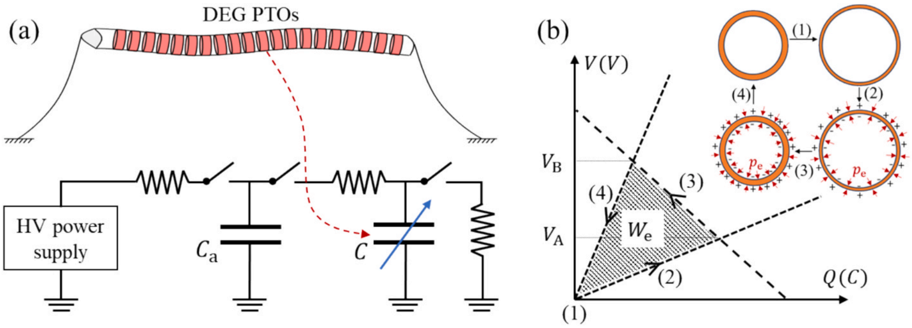

Fig. 6. (a) Control circuit for DEG PTO; (b) Schematic of the electrical energy generation cycle of a DEG unit.

deformation-dependent capacitance is coupled with auxiliary electrical components, including a fixed capacitance ($C_a = 394$ nF), resistive elements (R_1, R_2, and R_3), switching devices (S_1, S_2, and S_3), and a high-voltage (HV) power source, which together regulate the temporal evolution of voltage and charge during each conversion cycle.

In the present study, the DEG membranes are distributed continuously over the entire surface of the flexible tube. To account for spatial variations in deformation and electrical response, the PTO system is discretised along the tube length into 40 independently operating DEG units, each governed by the same control strategy. Considering a representative DEG unit, its energy conversion behaviour over one operating cycle is illustrated in Fig. 6(b), where the electrical charge Q and voltage V define the state of the system. The enclosed area W_e in the Q-V diagram corresponds to the net electrical energy generated during a single cycle. The conversion process can be conceptually divided into four successive stages: (1) expansion, (2) priming, (3) harvesting, and (4) discharging, corresponding to the typical operating cycle of dielectric elastomer generators. During expansion and priming, the membrane is mechanically stretched and electrically charged, whereas net electrical energy is generated during controlled contraction. A detailed description of each stage can be found in Ref. [33].

It is worth noting that net electrical energy generation occurs only during phases in which the DEG capacitance decreases, corresponding to the contraction of the flexible tube cross-section. In this stage, mechanical work performed against the electrostatic field is converted into electrical energy. By contrast, no net energy extraction takes place during the capacitance-increasing phase, when the tube cross-section expands. Accordingly, the control circuit applies voltage to the tube surface only during the contraction phase, thereby generating the electrostatic pressure required for energy conversion.

Based on the energy balance associated with the DEG conversion cycle, the instantaneous electrical power generated by the i-th DEG unit at position x is estimated as [33]

$$P_{e,i}(x,t) = \frac{1}{2}C(x,t+\Delta t)V^2(x,t+\Delta t) - \frac{1}{2}C(x,t)V^2(x,t)$$
$$+\frac{1}{2}C_a\left[V^2(x,t+\Delta t) - V^2(x,t)\right] \tag{7}$$

where $C(x,t)$ and $V(x,t)$ denote the capacitance and voltage of the i-th DEG unit at position x and time t, respectively. The average electrical power generated over one wave period T_w is defined as

$$\overline{P}_e = \frac{1}{T_w}\int_0^{T_w} P_e(t)\mathrm{d}t \tag{8}$$

The total mean electrical power output of the S3 WEC is obtained by summing the contributions from all DEG units distributed along the tube, i.e.

$$\overline{P}_t = \sum\nolimits_{i=1}^{40}\overline{P}_{e,i} \tag{9}$$

4.3. Computational domain, boundary conditions and mesh setup

A 3D numerical wave tank is constructed to simulate the flow field surrounding the S3 WEC, as shown in Fig. 7(a). The computational domain has dimensions of 6.5 m in length, 3 m in width, and 7.6 m in height. The water depth is set to 5 m, with an air layer of 1.5 m above the free surface. The S3 WEC is positioned at the centre of the domain to minimise boundary effects on the device response.

Although the downstream distance between the device and the outlet boundary is relatively short (2 m), an active wave absorption technique [34,35] is implemented at the outlet boundary to suppress wave reflections. This treatment allows the use of a compact computational domain while maintaining accurate wave conditions in the vicinity of the device. The effectiveness of this configuration has been demonstrated in our previous study [20], where the same numerical setup reproduced the target incident waves with negligible reflection near the WEC.

The mesh arrangement in the fluid domain is illustrated in Fig. 7(b). Local mesh refinement is applied in regions of interest to adequately resolve free surface evolution and deformation of the flexible tube. The minimum cell size is 0.01 D in the vicinity of the tube and 0.1 A_w near the free surface, where $D = 0.2$ m denotes the tube diameter and $A_w = 0.08$ m is the incident wave amplitude. The total number of cells in the computational domain is approximately 1.72 million.

At the inlet boundary, the velocity field is prescribed according to the incident wave parameters based on second-order Stokes wave theory. A

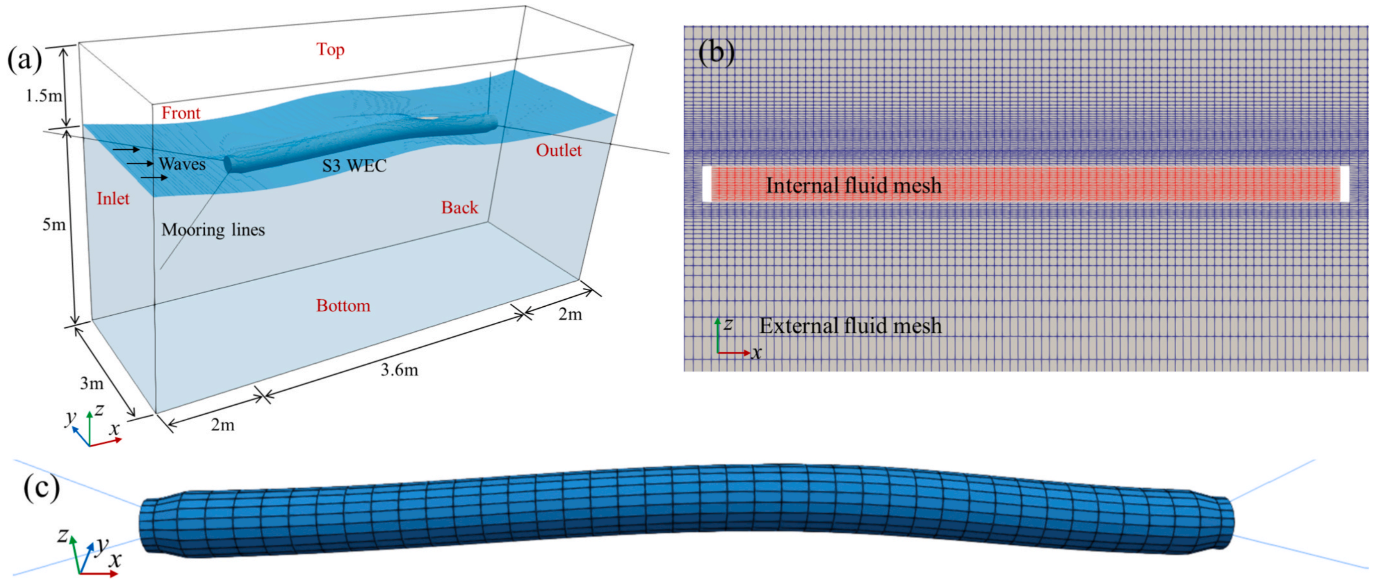

Fig. 7. (a) Computational domain for the flow field; (b) Mesh distribution in the internal and external fluid regions; (c) Structural model and finite element mesh of the flexible tube.

zero-gradient condition is imposed at the outlet, while the top boundary is treated as a pressure outlet. The seabed is modelled as a no-slip wall, and symmetry boundary conditions are applied on the front and back faces of the domain.

For the structural analysis, as illustrated in Fig. 7(c), the flexible tube is constrained at both ends by mooring lines, while its deformable surface is subjected to hydrodynamic and electrostatic loads. The structural mesh consists of 1876 eight-node brick elements (C3D8) [29], which are used to resolve the deformation of the tube under coupled FSE interactions.

To investigate the influence of key parameters on the coupled multiphysics response of the S3 WEC, a series of simulations is performed by varying wave conditions and electrical control parameters. Specifically, the effects of wave period, wave amplitude, initial voltage, and number of DEG layers are examined. The ranges of these parameters are selected with reference to the experimental study reported by Moretti et al. [33]. A summary of the simulation cases considered in this study is provided in Table 2.

Table 2
Summary of simulation cases.

No.	Wave period T_w(s)	Wave amplitude A_w(m)	Initial voltage V_0(kV)	Number of DEG layers n
Case 1	0.9 ~ 2.42	0.08	0	5
Case 2	0.9 ~ 2.42	0.08	5.0	5
Case 3	1.5	0.08 ~ 0.11	5.0	5
Case 4	1.5	0.08	1.0 ~ 6.0	5
Case 5	1.5	0.08	5.0	1 ~ 6

5. Results and discussion

This section presents a systematic analysis of the coupled FSE responses of the S3 WEC equipped with distributed DEG units. The influence of key parameters, including wave period, wave amplitude, initial voltage, and number of DEG layers, on the dynamic response and electrical power output of the system is examined. Subsection 5.1 first assesses mesh and time step independence to establish appropriate spatial and temporal resolutions for the numerical simulations. Subsection 5.2 investigates the coupled response of the S3 WEC under different wave periods, with particular emphasis on the interactions among the flow field, structural deformation, and electric field, as well as the role of electrostatic forces in the overall response. Subsections 5.3–5.5 subsequently explore the effects of wave amplitude, initial voltage, and number of DEG layers on the coupled system behaviour, focusing on both structural response and electrical power generation.

5.1. Mesh and time-step independence analysis

Mesh and time-step sensitivity analyses are conducted to determine appropriate spatial and temporal resolutions for the numerical simulations. Three mesh resolutions are considered, with minimum cell sizes near the tube of $2.0 \times 10^{-2}D$ (coarse mesh), $1.0 \times 10^{-2}D$ (medium mesh), and $5.0 \times 10^{-3}D$ (fine mesh). The corresponding total numbers of cells are approximately 1.21 million, 1.72 million, and 2.64 million, respectively. In addition, a time-step sensitivity analysis is performed on the medium mesh using time steps of $\Delta t = 2 \times 10^{-3}$ s, 1×10^{-3} s, and 5×10^{-4} s.

All sensitivity tests are carried out under regular wave conditions with a wave period of 1.5 s and a wave amplitude of 0.05 m. The initial voltage is set to 5.0 kV, and the number of DEG layers is fixed at 5. Fig. 8 presents the temporal evolution of the normalised tube cross-sectional area $S(x,t)/\overline{S}(x)$ at the mid-span location $x/L = 0.5$, where $S(x,t)$ denotes the instantaneous cross-sectional area of the tube and $\overline{S}(x)$ represents its time-averaged value at the same location.

The results indicate that the medium mesh yields predictions that are consistent with those obtained using the fine mesh, while requiring substantially lower computational cost. Similarly, a time step of 1×10^{-3} s provides a good compromise between numerical accuracy and efficiency. Based on these observations, the medium mesh combined with a time step of 1×10^{-3} s is adopted for all subsequent simulations.

5.2. Coupled response of the S3 WEC under different wave periods

This section investigates the coupled FSE response of the S3 WEC under different wave periods ($T_w = 0.9$ s ~ 2.42 s). Two scenarios are considered: a reference case without electrostatic pressure ($V_0 = 0$ kV, Case 1) and an electrostatically actuated case with initial voltage ($V_0 = 5$ kV, Case 2). In all simulations, the wave amplitude is fixed at $A_w/D = 0.4$, and the number of DEG layers is set to $n = 5$. By comparing the results of Case 1 and Case 2, the influence of electrostatic pressure on the

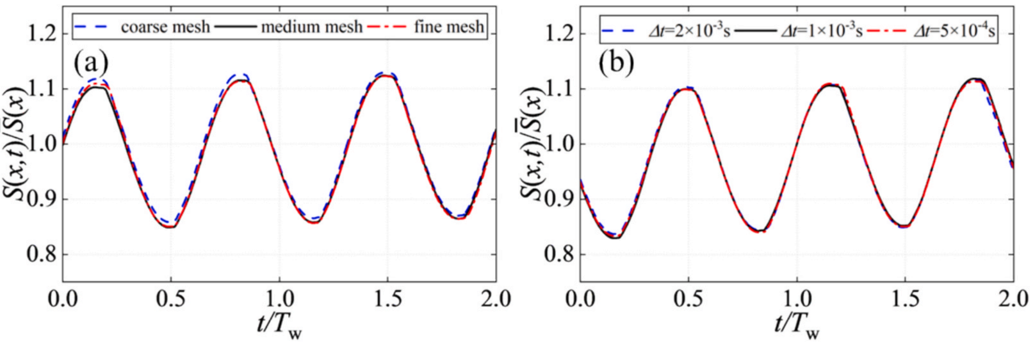

Fig. 8. Time histories of the normalised tube cross-sectional area $S(x,t)/\overline{S}(x)$ at $x/L = 0.5$: (a) mesh independence analysis; (b) time-step independence analysis.

multiphysics response of the system is systematically examined, including tube deformation modes, flow field characteristics, structural response, and electrical power generation of the S3 WEC.

5.2.1. *Tube deformation response*

As waves propagate over the flexible tube, the pressure difference across the tube wall induces periodic expansion and contraction of the tube cross-section. These local deformations propagate along the tube axis, forming travelling deformation patterns commonly referred to as bulge waves.

Fig. 9 illustrates the evolution of the tube cross-sectional area $S(x,t)$, normalised by the time-averaged cross-sectional area $\overline{S}(x)$, under different wave periods in the absence of electrostatic pressure. The numerical results capture multiple deformation modes of the tube, including the 1st-, 2nd-, and 3rd-order modes, as exemplified by Fig. 9 (l), 9(e), and 9(a), respectively.

Notably, no single pure deformation mode is observed at any given wave period. Instead, multiple deformation modes coexist over a wide range of wave conditions. This behaviour is closely associated with the 6DoF motions of the tube, particularly the surge motion. As reported by Babarit et al. [15], surge motion modifies the propagation speed of internal pressure waves within the tube, thereby altering its resonance characteristics. The present numerical observations are consistent with these experimental findings.

The influence of electrostatic pressure on tube deformation is illustrated in Fig. 10, which presents the deformation patterns under identical wave conditions with an initial voltage. For short wave periods (0.9 s $< T_w \leq 1.2$ s), where the 3rd-order deformation mode is dominant in the absence of electrostatic loading, the introduction of electrostatic pressure significantly modifies the deformation pattern, leading to the emergence of higher-order modes. In contrast, for longer wave periods (1.2 s $< T_w <$ 2.42 s), where the 1st- and 2nd-order modes prevail, the electrostatic pressure has a limited influence on the modal order. Instead, it primarily enhances the deformation amplitude while preserving the dominant deformation modes.

This trend is further quantified in Fig. 11, which compares the deformation amplitude of the tube cross-sectional area, $A_S(x)$, along the tube length under different wave periods, with and without electrostatic pressure. For all wave conditions considered, $A_S(x)$ is consistently larger when electrostatic pressure is applied. This amplification arises from the electrostatic pressure acting on both sides of the tube wall, which effectively reduces the structural stiffness of the tube. A similar stiffness-

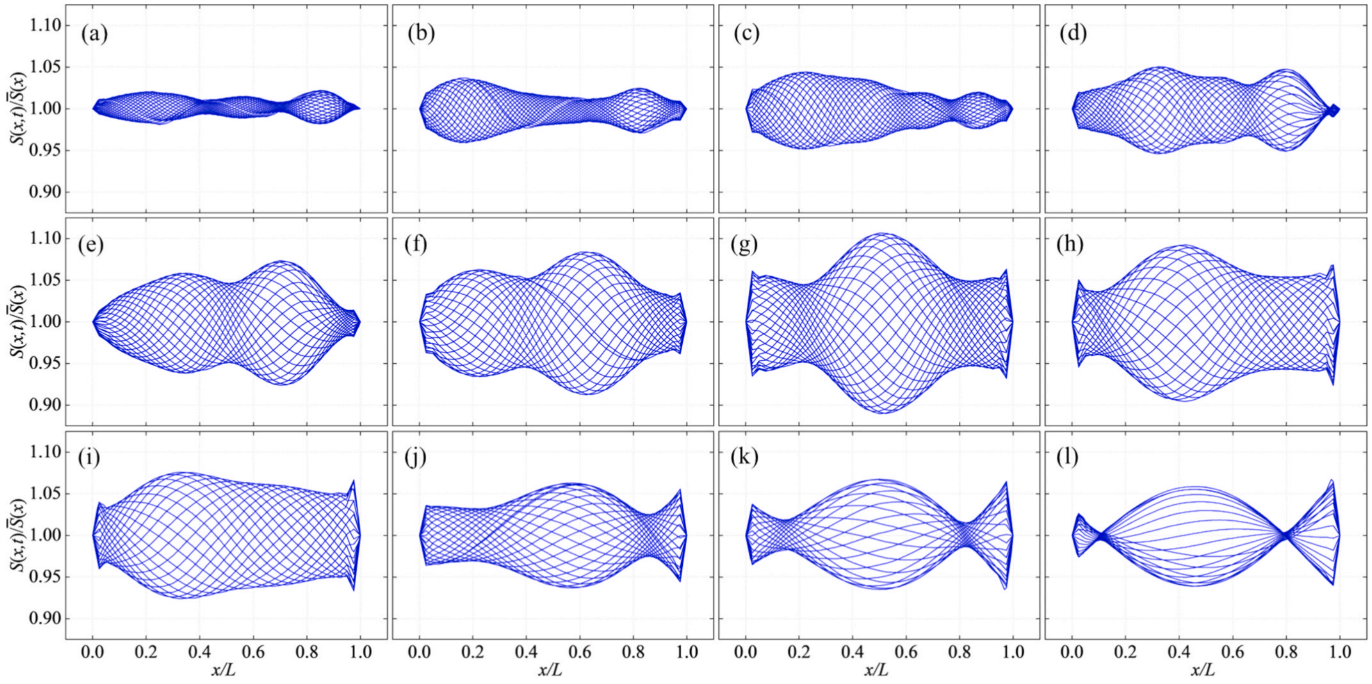

Fig. 9. Tube cross-sectional area $S(x,t)$, normalised by the time-averaged cross-sectional area $\overline{S}(x)$, at selected instants within one wave period for different wave periods, with no electrostatic pressure applied ($V_0 = 0$ kV): (a) $T_w = 0.9$ s; (b) $T_w = 1.0$ s; (c) $T_w = 1.1$ s; (d) $T_w = 1.2$ s; (e) $T_w = 1.32$ s; (f) $T_w = 1.4$ s; (g) $T_w = 1.5$ s; (h) $T_w = 1.62$ s; (i) $T_w = 1.7$ s; (j) $T_w = 1.9$ s; (k) $T_w = 2.1$ s; (l) $T_w = 2.42$ s.

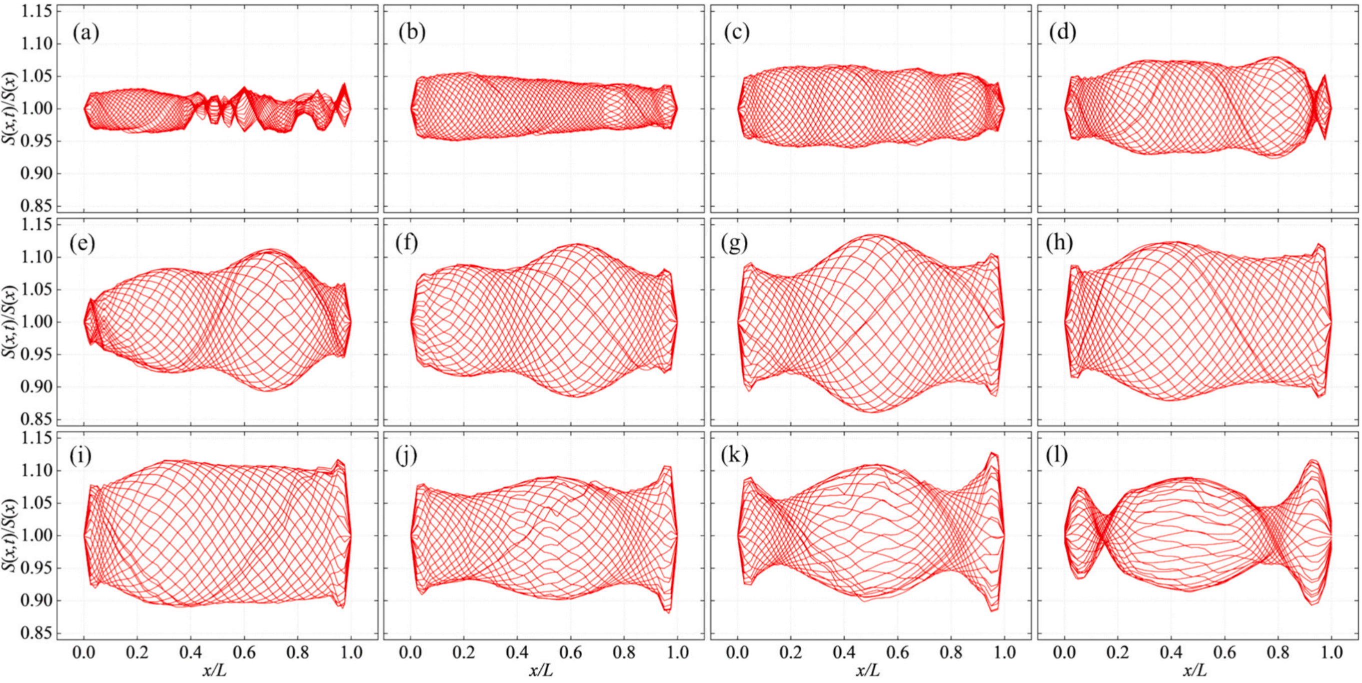

Fig. 10. Tube cross-sectional area $S(x,t)$, normalised by the time-averaged cross-sectional area $\bar{S}(x)$, at selected instants within one wave period for different wave periods, with electrostatic pressure applied ($V_0 = 5$ kV): (a) $T_w = 0.9$ s; (b) $T_w = 1.0$ s; (c) $T_w = 1.1$ s; (d) $T_w = 1.2$ s; (e) $T_w = 1.32$ s; (f) $T_w = 1.4$ s; (g) $T_w = 1.5$ s; (h) $T_w = 1.62$ s; (i) $T_w = 1.7$ s; (j) $T_w = 1.9$ s; (k) $T_w = 2.1$ s; (l) $T_w = 2.42$ s.

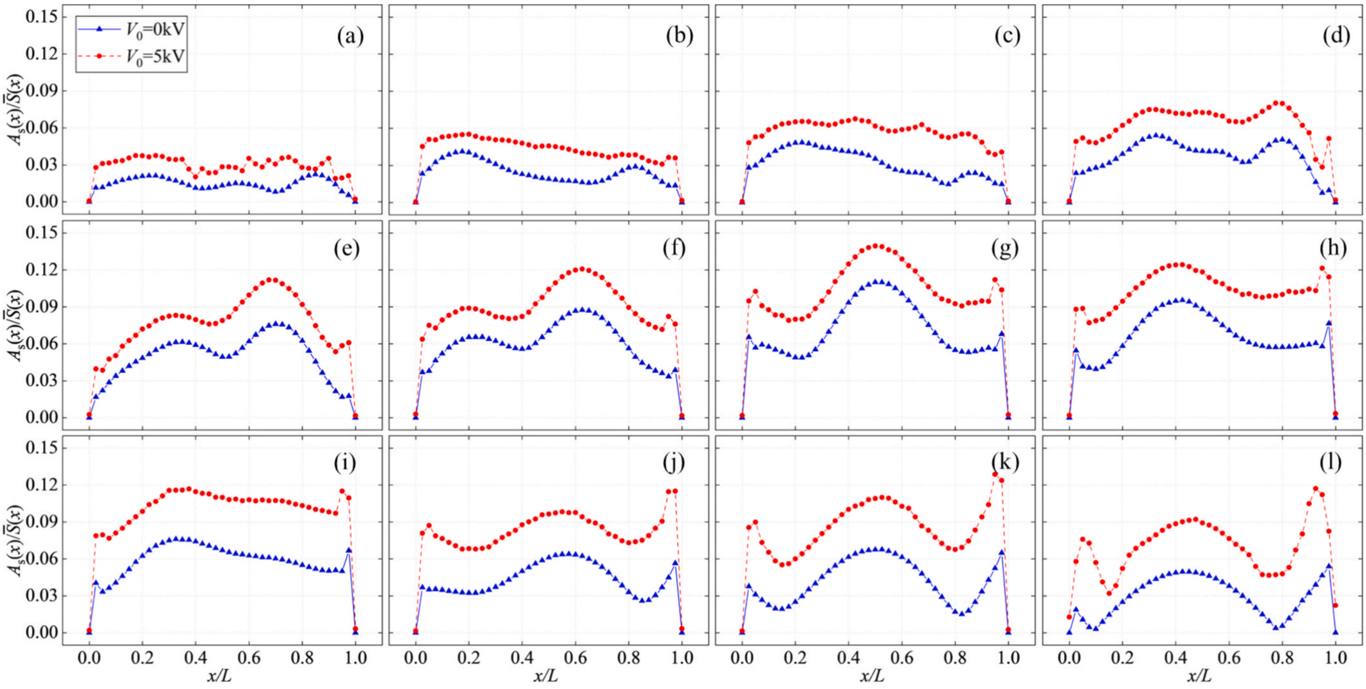

Fig. 11. Comparison of the deformation amplitude of the tube cross-sectional area, $A_S(x)$, normalised by the time-averaged cross-sectional area $\bar{S}(x)$, along the tube length for different wave periods, with and without electrostatic pressure: (a) $T_w = 0.9$ s; (b) $T_w = 1.0$ s; (c) $T_w = 1.1$ s; (d) $T_w = 1.2$ s; (e) $T_w = 1.32$ s; (f) $T_w = 1.4$ s; (g) $T_w = 1.5$ s; (h) $T_w = 1.62$ s; (i) $T_w = 1.7$ s; (j) $T_w = 1.9$ s; (k) $T_w = 2.1$ s; (l) $T_w = 2.42$ s.

softening effect induced by electrostatic loading has also been reported by Moretti et al. [33].

It should be noted that changes in the effective tube stiffness influence the propagation speed of bulge waves and, consequently, the resonance characteristics of the tube. This mechanism provides a plausible explanation for the observed shifts in dominant deformation modes at short wave periods (0.9 s $< T_w <$ 1.2 s) when electrostatic pressure is present.

5.2.2. *Fluid field response*

The fluid–structure interaction in the S3 WEC is highly complex. The flexible tube undergoes 6DoF motions and periodic deformation under the combined action of incident wave loading, mooring tension, and internal fluid hydrodynamics. These structural motions, in turn, strongly affect both the external wave field and the internal flow within the tube. Unlike reduced-order models [11,15], the present CFD-FEA-based FSE framework enables a direct and detailed visualisation of the coupled internal and external flow fields associated with the S3 WEC.

To illustrate the fluid–structure interaction under representative conditions, the case ($T_w = 1.5$ s) with the largest tube deformation amplitude is selected. Fig. 12 compares the interaction between the flexible tube and incident waves over one wave period for cases without ($V_0 = 0$ kV) and with electrostatic pressure ($V_0 = 5$ kV). It can be observed that the tube is not always fully submerged and intermittently emerges above the free surface. This intermittent emergence introduces pronounced nonlinear variations in the incident wave surface, as highlighted by the white dashed circles in Fig. 12, thereby altering the wave loading acting on the tube. Such nonlinear free-surface behaviour has been reported in experimental observations but cannot be captured by previously proposed linear numerical models [1,11,15].

A comparison between Fig. 12(a) and 12(b) indicates that the electrostatic pressure has a limited influence on the external wave field. Although the tube deformation amplitude increases when electrostatic pressure is applied, the resulting modification of the free-surface elevation remains relatively small. However, it is worth noting that the surge motion amplitudes of the tube bow and stern along the x-axis increase in the presence of electrostatic pressure, as illustrated in Fig. 13. This enhanced surge motion leads to larger deformation gradients along the tube length, which subsequently affects the overall deformation shape of the tube.

To further investigate the internal flow dynamics, the pressure distribution inside the tube is examined for the same wave period ($T_w = 1.5$ s). Fig. 14 presents the pressure field within the tube on the x-z plane at selected instants over one wave period. The pressure distribution along the z-axis generally increases with depth, consistent with hydrostatic effects. However, the pressure variation along the x-axis does not directly correlate with the instantaneous submergence depth at a given axial location. A representative example is observed at $t/T_w = 0.25$, where the submergence depth at $x/L = 0.5$ is larger than that at $x/L = 0$ and $x/L = 1$, yet the pressure at the tube centre is lower. This behaviour arises because the tube cross-section at $x/L = 0.5$ is compressed at this instant (Fig. 15), driving internal fluid towards both ends of the tube and increasing the pressure at the tube ends despite the smaller submergence depth.

Further insight is obtained by examining the pressure distribution on the y-z plane at the mid-length section ($x/L = 0.5$), as shown in Fig. 15. At a given instant, the pressure generally increases with depth along the z-axis. However, comparing different instants within the wave period reveals that the overall pressure level is strongly influenced by the instantaneous deformation state of the tube. For example, although the section is submerged deeper at $t/T_w = 0.5$ than at $t/T_w = 0.75$, the pressure is lower at $t/T_w = 0.5$. Meanwhile, the tube cross-sectional area is larger at $t/T_w = 0.75$, which facilitates internal fluid accumulation and leads to a higher local pressure level. These observations demonstrate that while the pressure distribution on a given cross-section is affected by submergence depth (along the z-axis), the axial pressure variation (along the x-axis) is primarily governed by tube deformation and the associated internal flow redistribution.

In addition, comparisons between Fig. 14(a) and 14(b), as well as Fig. 15(a) and 15(b), show that the application of electrostatic pressure leads to a slight overall reduction in the internal pressure field, both in the x-z and y-z planes. This reduction is mainly attributed to the increased tube deformation amplitude, which leads to a reduction in pressure accumulation. Nevertheless, the overall influence of electrostatic pressure on the internal pressure field remains relatively modest.

5.2.3. *Structural stress response*

The stress distribution on the tube surface is analysed for the wave period $T_w = 1.5$ s associated with the maximum tube cross-sectional deformation amplitude. Fig. 16 presents the von Mises stress (σ_v) distribution on the tube surface at selected instants over one wave period. The regions of maximum stress at each instant are highlighted by black dashed boxes. As time progresses from $t/T_w = 0$ to $t/T_w = 0.75$, the location of the maximum stress clearly migrates from the left end of the tube to the right end. This evolution closely follows the propagation of the maximum cross-sectional deformation along the tube length, thereby providing a clear visualisation of the bulge wave propagation process.

A comparison between Fig. 16(a) and 16(b) indicates that the overall stress level on the tube surface is significantly reduced when electrostatic pressure is applied. As discussed earlier, the electrostatic pressure effectively reduces the structural stiffness of the tube. Consequently, although the cross-sectional deformation amplitude increases, the corresponding maximum stress decreases under the same wave conditions.

However, this stress-reduction effect does not persist across all wave periods. As shown in Fig. 17(a), for $0.9 \text{ s} < T_w < 1.7$ s, the maximum σ_v on the tube is lower when electrostatic pressure is applied. In contrast, for longer wave periods ($1.7 \text{ s} < T_w < 2.42$ s), the maximum σ_v increases despite the presence of electrostatic pressure.

This trend is closely associated with the magnitude of cross-sectional

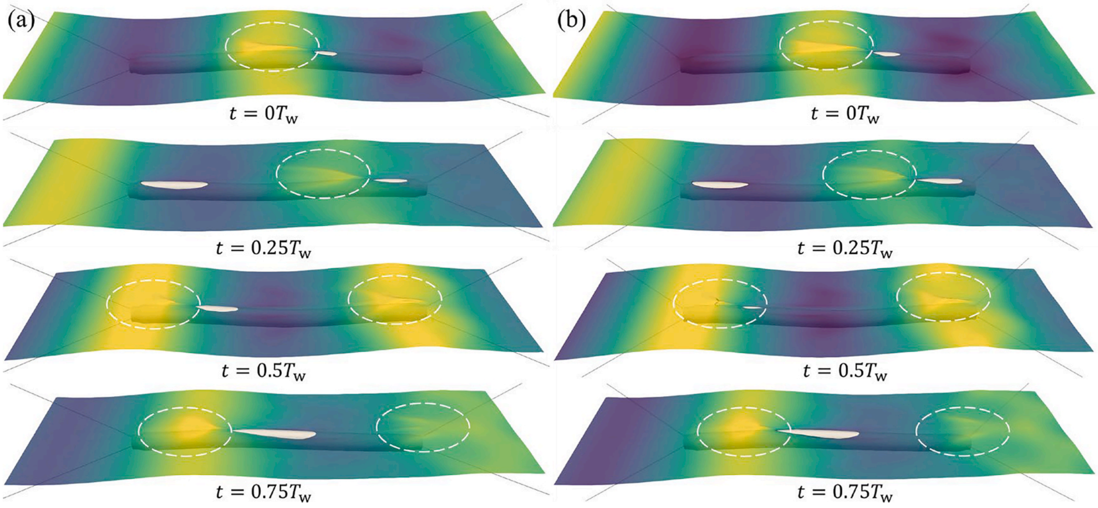

Fig. 12. Interaction between the flexible tube and incident waves at selected instants within one wave period for $T_w = 1.5$ s: (a) $V_0 = 0$ kV; (b) $V_0 = 5$ kV.

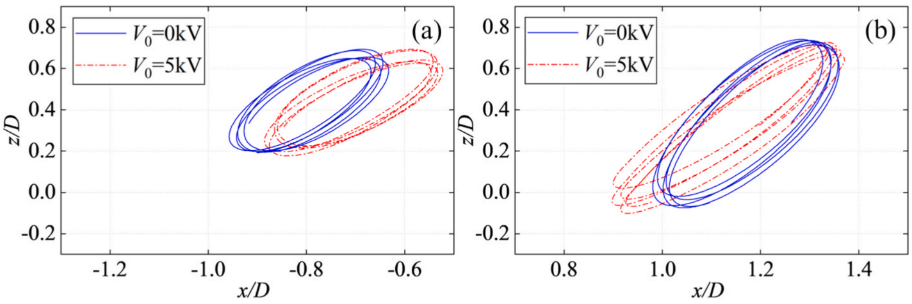

Fig. 13. Trajectories of the tube ends at $T_\mathrm{w} = 1.5$ s for $V_0 = 0$ kV and $V_0 = 5$ kV: (a) bow; (b) stern.

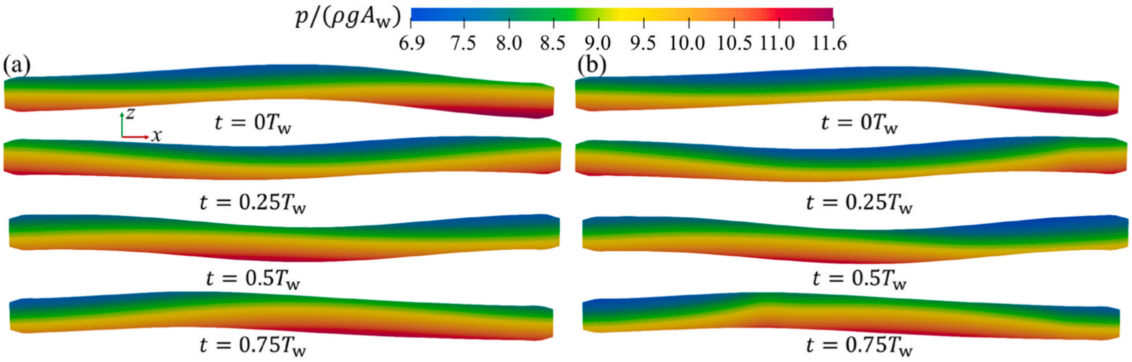

Fig. 14. Internal pressure distribution on the x-z plane at selected instants over one wave period ($T_\mathrm{w} = 1.5$ s): (a) $V_0 = 0$ kV; (b) $V_0 = 5$ kV.

deformation induced by electrostatic loading. As indicated in Fig. 17(b), the ratio between the maximum cross-sectional deformation amplitude with electrostatic pressure, $A_\mathrm{S}^\mathrm{max}(x)$, and that without electrostatic pressure, $A_\mathrm{S}'^\mathrm{max}(x)$, is plotted as a function of wave period. For $1.7\ \mathrm{s} < T_\mathrm{w} < 2.42$ s, the application of electrostatic pressure increases the maximum deformation amplitude by more than 80%. Under these conditions, although electrostatic pressure leads to an effective reduction in tube stiffness, the substantial increase in deformation dominates the stress response, resulting in an overall increase in the maximum σ_v.

5.2.4. Electrical power generation

As described in Section 4.2, the control circuit applies voltage only during the contraction phase of the tube cross-section, such that the embedded DEG units generate net electrical energy. Fig. 18(a) and 18(c) present the spatiotemporal distributions of the normalised tube cross-sectional area, $S(x,t)/\overline{S}(x)$, for two representative wave periods ($T_\mathrm{w} = 1.5$ s and $T_\mathrm{w} = 2.42$ s). For both wave conditions, the cross-sectional area at different axial locations varies periodically over time. Consequently, for a given cross-section, voltage is applied only during the half-cycle in which the cross-sectional area decreases, and the tube is subjected to electrostatic pressure during this phase, as illustrated in Fig. 18(b) and 18(d).

When $S(x,t)$ starts to decrease, the control circuit applies voltage to the corresponding DEG units, leading to the maximum electrostatic pressure at the onset of the contraction phase. As $S(x,t)$ continues to decrease towards its minimum value, the electrostatic pressure gradually diminishes. Net electrical energy is therefore generated only during the contraction phase of the tube cross-section.

Along the length of the S3 WEC, multiple DEG units are distributed continuously. As long as local cross-sectional contraction occurs, the corresponding DEG units generate net electrical energy. Fig. 19 illustrates the spatiotemporal distribution of the instantaneous electrical power output of the distributed DEG units, $P_\mathrm{e}(x,t)$, together with the total instantaneous electrical power of the S3 WEC, P_t. For both the shorter ($T_\mathrm{w} = 1.5$ s) and longer ($T_\mathrm{w} = 2.42$ s) wave periods, multiple DEG units operate simultaneously along the tube length, continuously producing net electrical power. As a result, P_t remains positive throughout the entire wave cycle, as shown in Fig. 19(b) and 19(d). This highlights a key advantage of the S3 WEC with a distributed PTO configuration over flexible OWC WECs employing a single DEG unit [33], namely its ability to maintain a continuously positive net electrical power output. In addition, P_t exhibits a periodic variation in time, following the wave-induced deformation dynamics of the tube.

To further quantify the power generation performance, the time-averaged electrical power $\overline{P}_\mathrm{t}$ of the S3 WEC under different wave periods is shown in Fig. 20. As the wave period increases from $T_\mathrm{w} = 0.9$ s to $T_\mathrm{w} = 1.5$ s, $\overline{P}_\mathrm{t}$ increases monotonically, whereas a decreasing trend is observed for longer wave periods ($1.5\ \mathrm{s} < T_\mathrm{w} < 2.42$ s). By comparing these results with the tube deformation amplitude under different wave periods (Fig. 11), it can be concluded that, overall, the time-averaged electrical power increases with increasing tube deformation amplitude.

5.3. Effect of wave amplitude on the coupled system response

The influence of incident wave amplitude on the coupled FSE response of the S3 WEC is examined through a series of simulations with varying wave amplitudes ($A_\mathrm{w}/D = 0.4 \sim 0.55$, Case 3). In all simulations, the wave period is fixed at $T_\mathrm{w} = 1.5$ s, corresponding to the condition that yields the maximum tube deformation amplitude. The initial voltage is set to $V_0 = 5$ kV, and the number of DEG layers is fixed at $n = 5$. The following analysis focuses on the effects of wave amplitude on the fluid field, structural deformation, stress response, and electrical power generation of the S3 WEC.

5.3.1. Fluid field response

As the wave amplitude increases, the interaction between the flexible tube and the free surface becomes more pronounced. Fig. 21 illustrates the interaction between the flexible tube and the incident waves at selected instants within one wave period for $A_\mathrm{w}/D = 0.55$. Compared with the case of $A_\mathrm{w}/D = 0.4$ shown in Fig. 12(b), the nonlinear

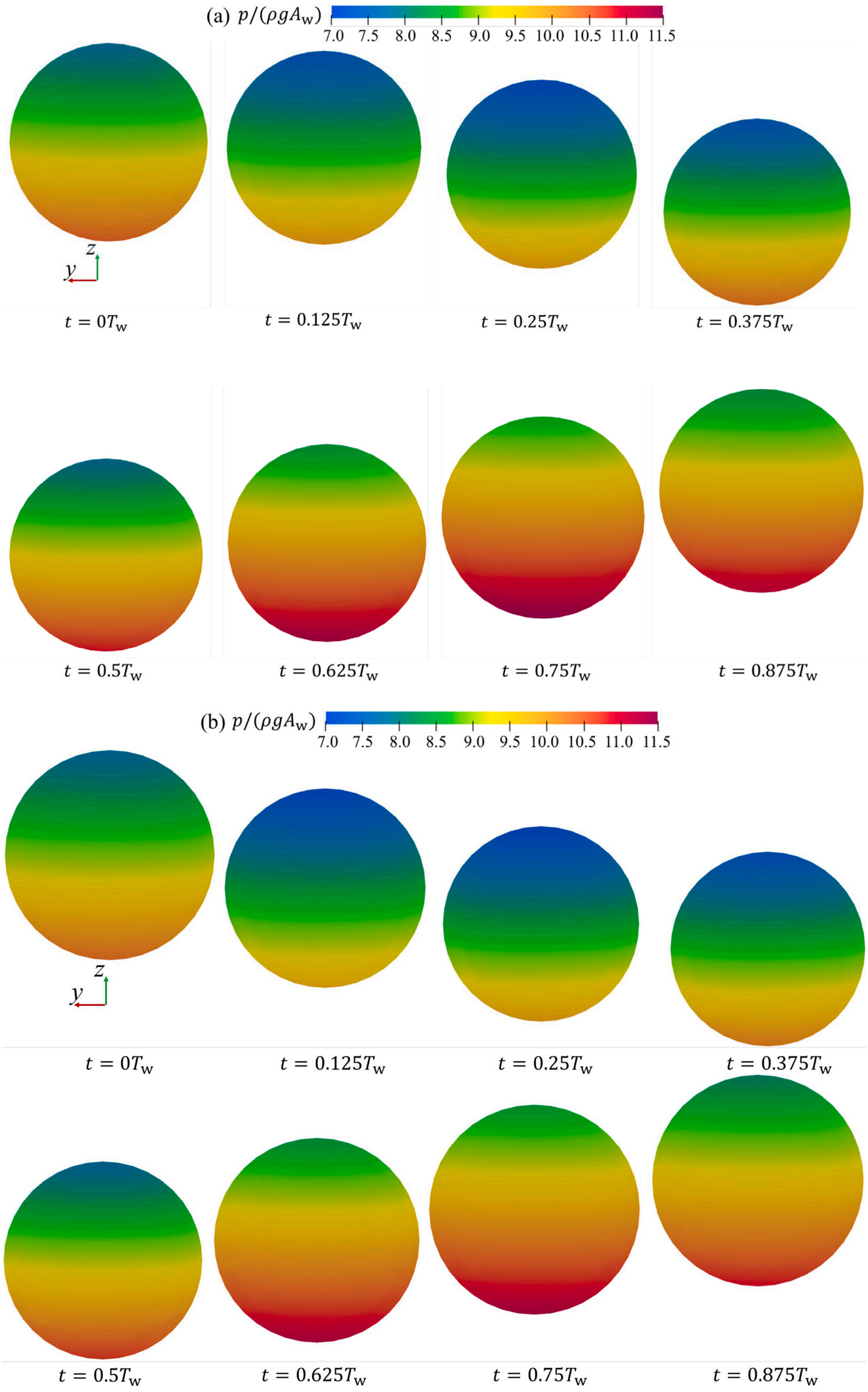

Fig. 15. Pressure distribution on the *y*-*z* plane at the mid-length section ($x/L = 0.5$) at selected instants over one wave period ($T_\mathrm{w} = 1.5$ s): (a) $V_0 = 0$ kV; (b) $V_0 = 5$ kV.

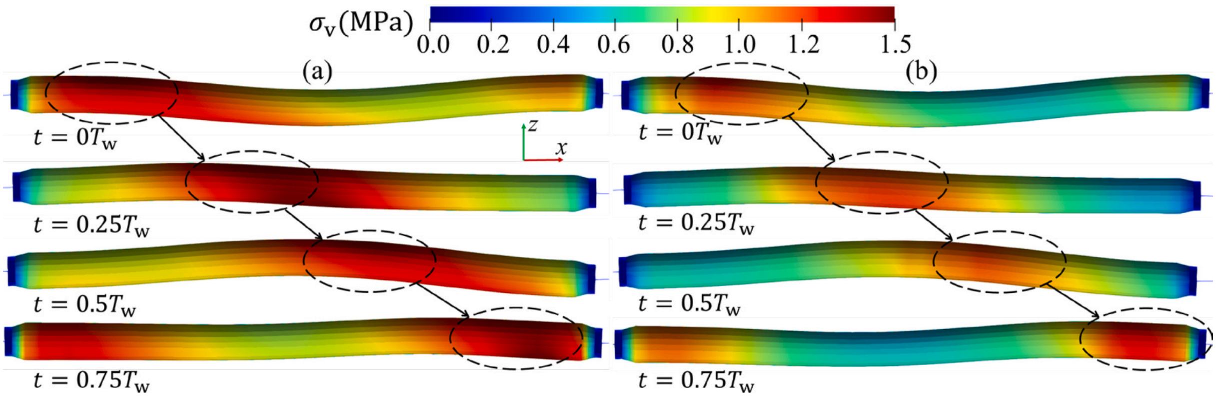

Fig. 16. Von Mises stress distribution on the tube surface at selected instants over one wave period ($T_w = 1.5$ s): (a) $V_0 = 0$ kV; (b) $V_0 = 5$ kV.

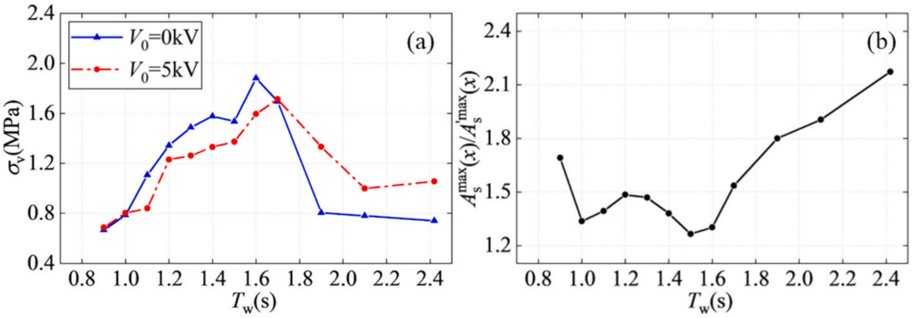

Fig. 17. (a) Comparison of the maximum von Mises stress σ_v on the tube under different wave periods for $V_0 = 0$ kV and $V_0 = 5$ kV. (b) Ratio between the maximum cross-sectional deformation amplitude with electrostatic pressure, $A_S^{max}(x)$, and that without electrostatic pressure, $A_S'^{max}(x)$, as a function of wave period.

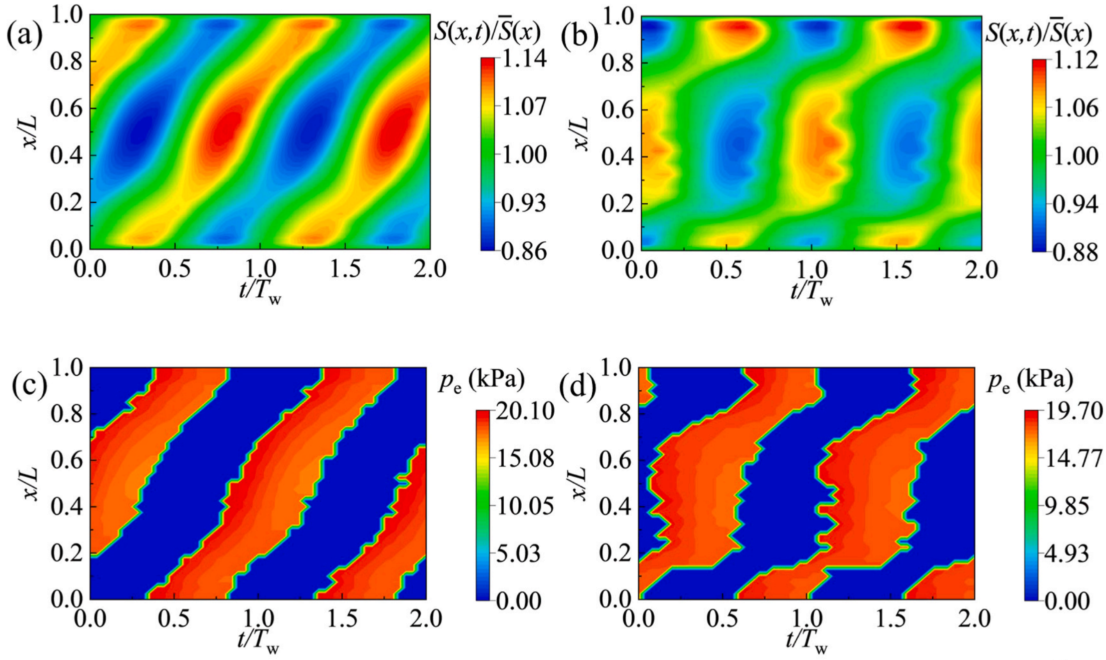

Fig. 18. Spatiotemporal distributions of the normalised tube cross-sectional area, $S(x,t)/\overline{S}(x)$, and electrostatic pressure p_e: (a) $S(x,t)/\overline{S}(x)$, $T_w = 1.5$ s; (b) p_e, $T_w = 1.5$ s; (c) $S(x,t)/\overline{S}(x)$, $T_w = 2.42$ s; (d) p_e, $T_w = 2.42$ s.

deformation of the wave surface becomes significantly more evident due to the enhanced 6DoF motions of the tube, as highlighted by the white dashed circles. In addition, a larger portion of the tube intermittently emerges above the free surface, which is expected to have a more pronounced influence on the hydrodynamic loading acting on the structure. Both the intensified free-surface nonlinearity and the increased extent of tube emergence are challenging to capture accurately using linear numerical models or reduced-order models [11,15].

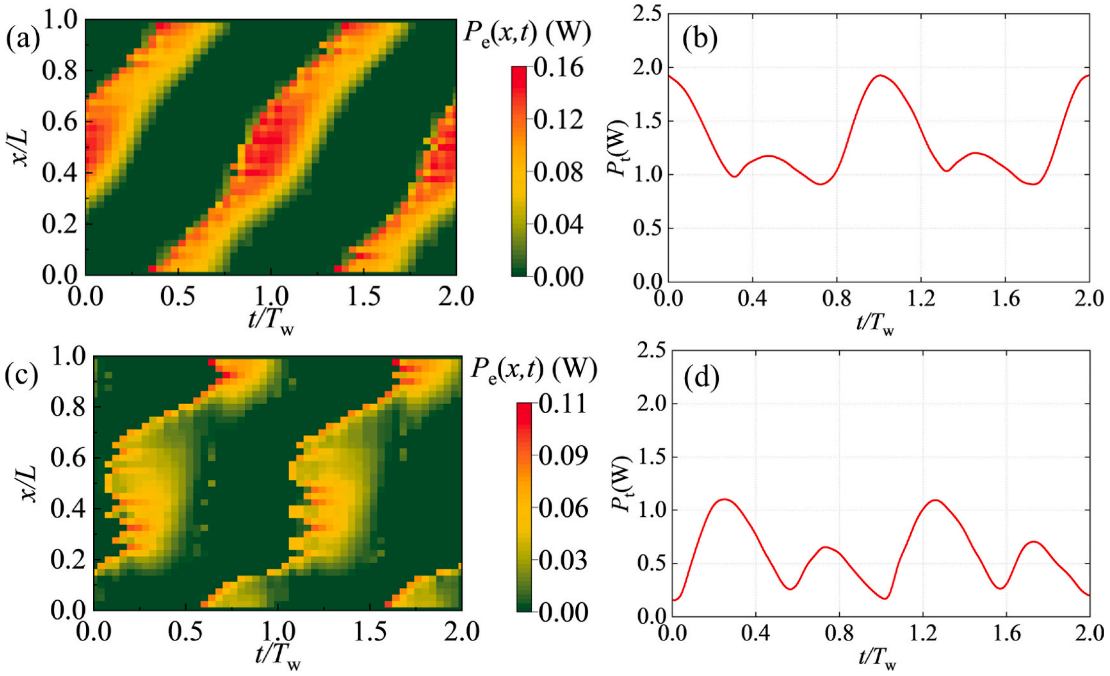

Fig. 19. Spatiotemporal distributions of the instantaneous electrical power output of the distributed DEG units, $P_e(x,t)$, and the instantaneous power of the S3 WEC, P_t: (a) $P_e(x,t)$, $T_w = 1.5$ s; (b) P_t, $T_w = 1.5$ s; (c) $P_e(x,t)$, $T_w = 2.42$ s; (d) P_t, $T_w = 2.42$ s.

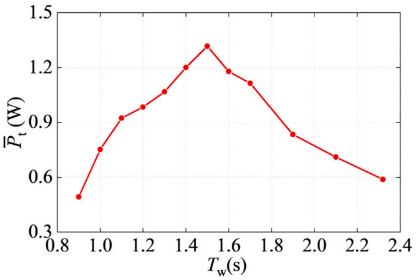

Fig. 20. Time-averaged electrical power $\overline{P}_t$ of the S3 WEC under different wave periods.

These observations highlight the necessity of high-fidelity FSE modelling when assessing the S3 WEC response under increased wave excitation.

In addition to the enhanced free-surface deformation, increasing wave amplitude leads to larger 6DoF motions of the tube, particularly in surge and heave. As illustrated in Fig. 22, when A_w/D increases from 0.4 to 0.55, the surge motion amplitudes of the tube bow and stern along the x-axis increase by 32.2% and 48.1%, respectively, indicating more pronounced axial deformation along the tube length. Meanwhile, the heave motion amplitudes of the bow and stern along the z-axis increase by 64.8% and 42.9%, respectively, over the same range of wave amplitudes.

5.3.2. *Structural response*

Fig. 23 presents the deformation characteristics of the flexible tube under different wave amplitudes. It can be observed that the deformation mode of the tube remains unchanged as the wave amplitude increases, with the response being dominated by the 2nd-order deformation mode. However, the deformation amplitude of the tube cross-sections distributed along the tube length, $A_S(x)$, increases markedly with increasing wave amplitude, as quantified in Fig. 24(a).

Taking the mid-length cross-section ($x/L = 0.5$), where the maximum deformation occurs, as an example, the normalised deformation amplitude $A_S(x)/\overline{S}(x)$ increases from 0.139 to 0.177 as A_w/D increases from 0.4 to 0.55, corresponding to an increase of 27.3%. The increase in $A_S(x)$ is accompanied by a corresponding increase in the structural stress level. As shown in Fig. 24(b), the maximum von Mises stress (σ_v) on the tube surface increases from 1.37 MPa to 1.72 MPa over the same range of wave amplitudes, representing an increase of 25.5%.

5.3.3. *Electrical power generation*

Fig. 25 presents the spatiotemporal distributions of the electrostatic

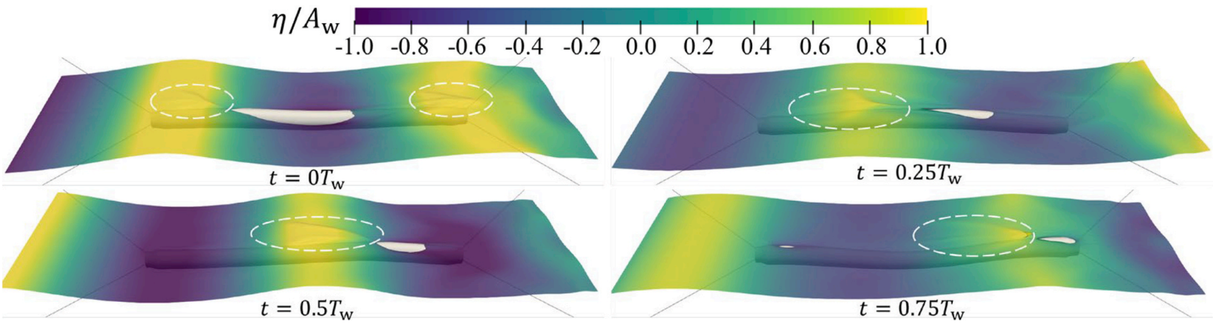

Fig. 21. Interaction between the flexible tube and incident waves at selected instants within one wave period for $T_w = 1.5$ s, $A_w/D = 0.55$, and $V_0 = 5$ kV.

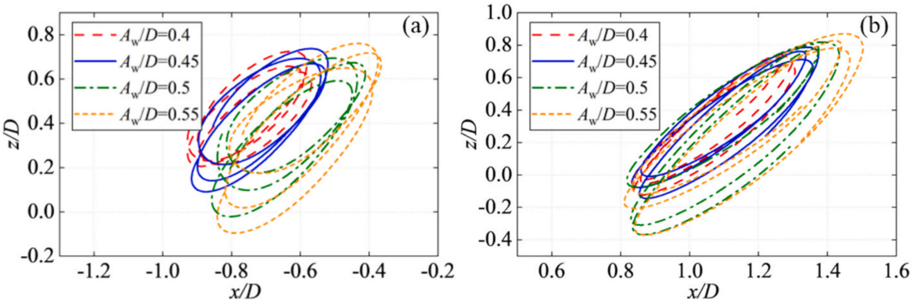

Fig. 22. Comparison of the motion trajectories of the tube ends under different wave amplitudes at $T_w = 1.5$ s and $V_0 = 5$ kV: (a) bow; (b) stern.

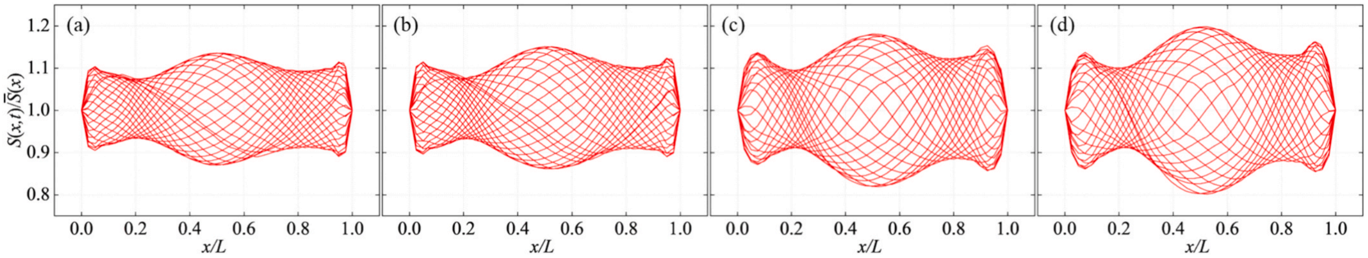

Fig. 23. Tube cross-sectional area $S(x,t)$, normalised by the time-averaged cross-sectional area $\bar{S}(x)$, at selected instants within one wave period for different wave amplitudes at $T_w = 1.5$ s and $V_0 = 5$ kV: (a) $A_w/D = 0.4$; (b) $A_w/D = 0.45$; (c) $A_w/D = 0.5$; (d) $A_w/D = 0.55$.

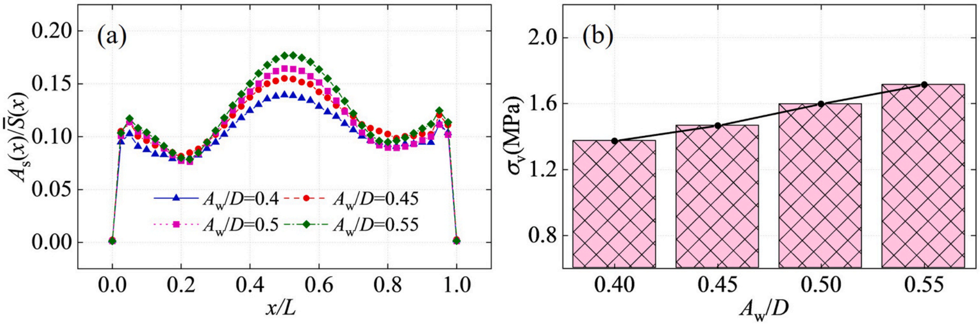

Fig. 24. (a) Deformation amplitude of the tube cross-sectional area, $A_S(x)$, normalised by $\bar{S}(x)$, under different wave amplitudes at $T_w = 1.5$ s and $V_0 = 5$ kV; (b) Maximum von Mises stress, σ_v, on the tube as a function of wave amplitude at $T_w = 1.5$ s and $V_0 = 5$ kV.

pressure p_e acting on the tube surface under different wave amplitudes. As discussed previously, an increase in wave amplitude leads to a larger tube deformation amplitude. The enhanced deformation induces more pronounced variations in the thickness of the embedded DEG layers (t_m), which, according to Eq. (6), results in higher p_e.

As p_e increases, more mechanical work is performed against the electric field during tube contraction, leading to higher electrical power output from the S3 WEC. Fig. 26(a) shows the temporal variation of the instantaneous electrical power P_t under different wave amplitudes. The instantaneous power exhibits a periodic variation in time, and its variation amplitude increases with increasing wave amplitude. Specifically, when A_w/D increases from 0.4 to 0.55, the variation amplitude of P_t increases by approximately 36.4%.

Furthermore, the time-averaged electrical power $\bar{P}_t$ under different wave amplitudes is presented in Fig. 26(b). As A_w/D increases from 0.4 to 0.55, $\bar{P}_t$ rises from 1.32 W to 1.68 W. These results demonstrate that increasing wave amplitude enhances the electrical power generation of the S3 WEC by amplifying tube deformation, but also leads to more

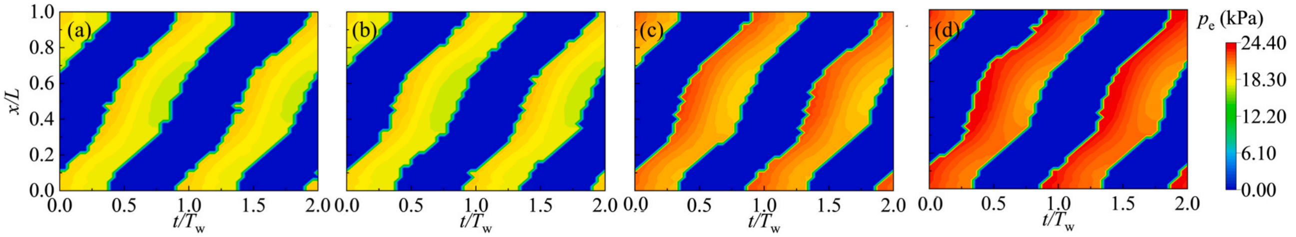

Fig. 25. Spatiotemporal distributions of the electrostatic pressure p_e acting on the tube surface under different wave amplitudes at $T_w = 1.5$ s and $V_0 = 5$ kV: (a) $A_w/D = 0.4$; (b) $A_w/D = 0.45$; (c) $A_w/D = 0.5$; (d) $A_w/D = 0.55$.

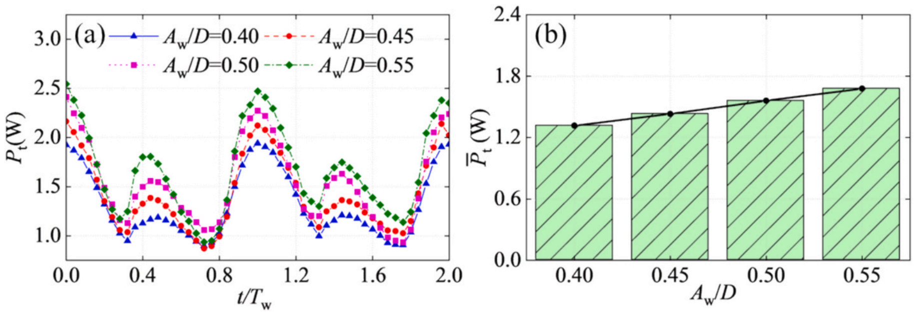

Fig. 26. Electrical power generation of the S3 WEC under different wave amplitudes at $T_w = 1.5$ s and $V_0 = 5$ kV: (a) Instantaneous electrical power P_t; (b) Time-averaged electrical power $\overline{P}_t$.

pronounced temporal variations in the power output. This trend further suggests that stronger wave excitation improves electrical output at the expense of higher structural loading and output variability, and therefore should be considered within wave-condition-dependent survivability limits in practical operation.

5.4. Effect of initial voltage on structural response and power output

The applied voltage directly governs the electrostatic pressure acting on the tube, thereby modifying its mechanical response and, consequently, the electrical power output of the S3 WEC. To investigate this effect, a series of numerical simulations with varying initial voltage ($V_0 = 1 \sim 6$ kV) are performed (Case 4). The wave period is fixed at $T_w = 1.5$ s, the wave amplitude is set to $A_w/D = 0.4$, and the number of DEG layers is fixed at $n = 5$. As discussed in the previous section, for this selected wave period, the electrostatic pressure has a limited influence on both the internal and external flow fields. Therefore, the flow field response is not further discussed here. The following analysis focuses on the effects of voltage magnitude on the structural stress response and electrical power generation of the S3 WEC.

5.4.1. Structural response

As indicated by Eq. (6), the electrostatic pressure p_e acting on the tube is proportional to the square of the voltage V_0. Consequently, increasing V_0 leads to a pronounced increase in p_e, as shown in Fig. 27. However, the increase in electrostatic pressure does not alter the deformation mode of the tube. As illustrated in Fig. 28, the tube deformation remains dominated by the 2nd-order mode over the entire range of initial voltages considered.

Despite the unchanged deformation mode, the deformation amplitude of the tube cross-sections distributed along the tube length increases significantly with increasing initial voltage, as quantified in Fig. 29(a). Taking the mid-length cross-section ($x/L = 0.5$) as an example, the normalised deformation amplitude $A_S(x)/\overline{S}(x)$ increases from 0.112 to 0.144 as V_0 increases from 1 kV to 6 kV, corresponding to an increase of 28.6%. The enhancement in deformation amplitude is accompanied by a corresponding increase in structural stress. As shown in Fig. 29(b), the maximum von Mises stress σ_v on the tube surface increases from 1.26 MPa to 1.52 MPa over the same voltage range, representing an increase of 20.6%.

5.4.2. Electrical power generation

The initial voltage influences the electrical power output of the S3 WEC through two primary mechanisms. First, as discussed above, increasing V_0 enhances the tube deformation amplitude, thereby amplifying the capacitance variation of the embedded DEG units. Second, according to Eq. (6), the electrical power output exhibits a direct quadratic dependence on the applied voltage.

Fig. 30(a) shows the temporal variation of the instantaneous electrical power P_t under different initial voltages. It can be observed that the variation amplitude of P_t increases markedly with increasing V_0. Specifically, as V_0 increases from 1 kV to 6 kV, the variation amplitude of P_t increases by approximately a factor of 36. The time-averaged electrical power $\overline{P}_t$ also increases rapidly with increasing initial

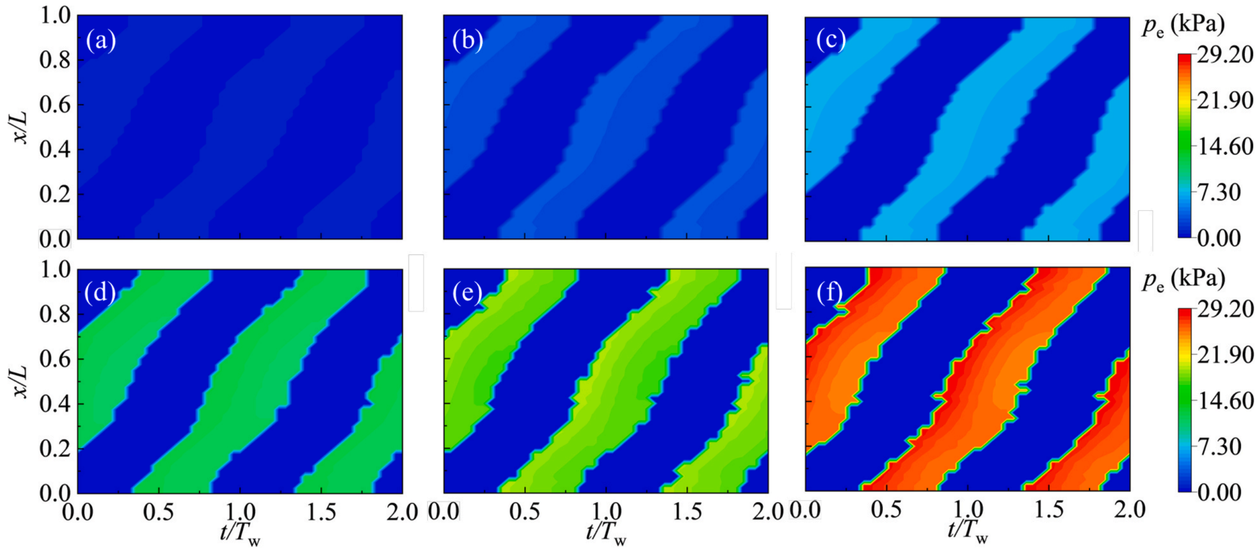

Fig. 27. Spatiotemporal distributions of the electrostatic pressure p_e acting on the tube surface under different initial voltages at $T_w = 1.5$ s: (a) $V_0 = 1$ kV; (b) $V_0 = 2$ kV; (c) $V_0 = 3$ kV; (d) $V_0 = 4$ kV; (e) $V_0 = 5$ kV; (f) $V_0 = 6$ kV.

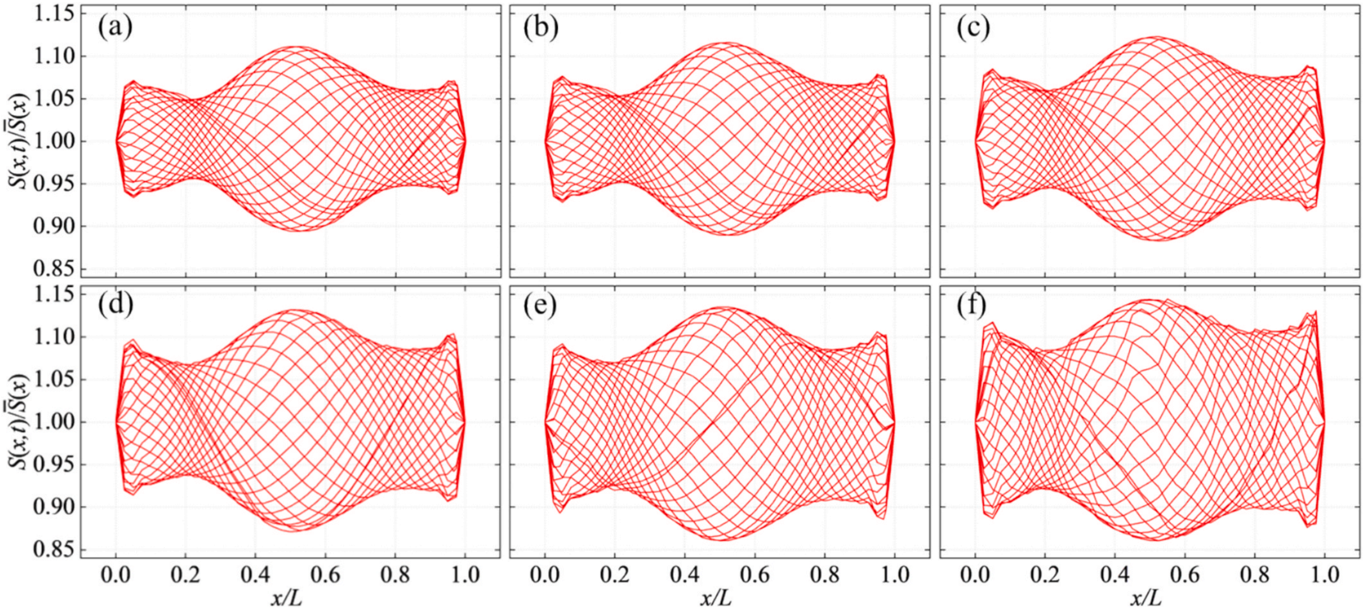

Fig. 28. Tube cross-sectional area $S(x,t)$, normalised by the time-averaged cross-sectional area $\overline{S}(x)$, at selected instants within one wave period for different initial voltages at $T_w = 1.5$ s: (a) $V_0 = 1$ kV; (b) $V_0 = 2$ kV; (c) $V_0 = 3$ kV; (d) $V_0 = 4$ kV; (e) $V_0 = 5$ kV; (f) $V_0 = 6$ kV.

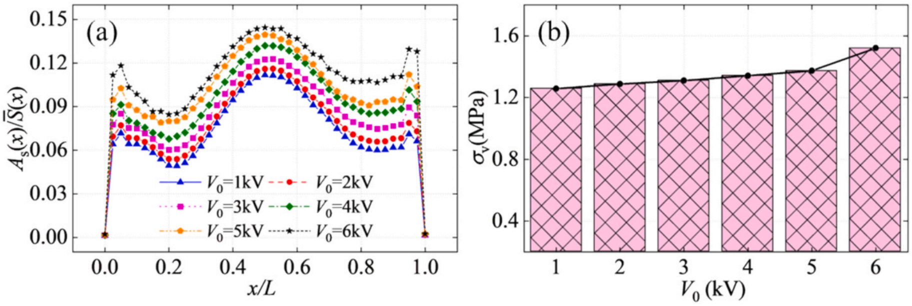

Fig. 29. (a) Deformation amplitude of the tube cross-sectional area, $A_S(x)$, normalised by $\overline{S}(x)$, under different initial voltages at $T_w = 1.5$ s; (b) Maximum von Mises stress σ_v on the tube as a function of initial voltage.

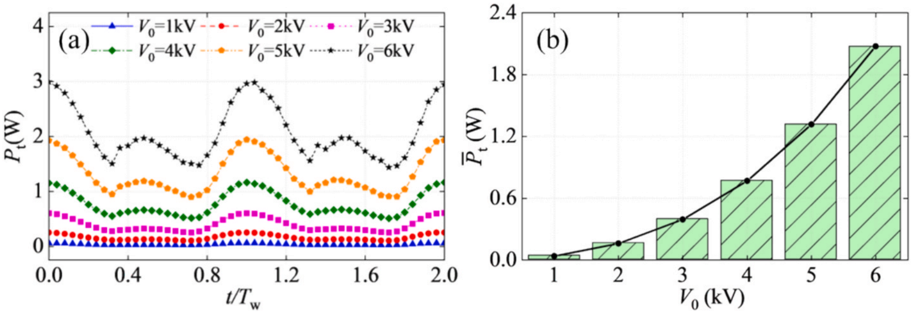

Fig. 30. Electrical power generation of the S3 WEC under different initial voltages at $T_w = 1.5$ s: (a) Instantaneous electrical power P_t; (b) Time-averaged electrical power $\overline{P}_t$.

voltage, following an approximately quadratic trend, as shown in Fig. 30 (b). Over the same voltage range, $\overline{P}_t$ increases from 0.038 W to 2.1 W, corresponding to an approximately 55-fold increase.

These results reveal a clear trade-off between electrical power enhancement and structural loading as the initial voltage increases. Although a higher initial voltage can significantly improve the mean electrical power output, it also increases structural stress and output fluctuation. This suggests that the initial voltage should not be maximised indiscriminately in practical operation, but instead selected within stress-constrained operating ranges. Under more energetic sea states, adaptive voltage limitation may provide a practical means of mitigating excessive structural loading while retaining acceptable energy capture performance.

5.5. Effect of the number of DEG layers on power generation performance

The number of DEG layers influences the electromechanical behaviour of the S3 WEC by modifying the electrostatic pressure acting on the tube wall, which in turn affects tube deformation and electrical power output. To investigate this effect, a series of numerical simulations with varying numbers of DEG layers ($n = 1 \sim 6$, Case 5) are conducted. The wave period is fixed at $T_w = 1.5$ s, the wave amplitude is set to $A_w/D = 0.4$, and the initial voltage is maintained at $V_0 = 5$ kV. The following analysis focuses on how the number of DEG layers affects the structural stress response and electrical power generation of the S3 WEC.

5.5.1. Structural response

According to Eq. (6), the electrostatic pressure p_e acting on the tube surface scales with the square of the number of DEG layers n, in a manner analogous to its dependence on the initial voltage V_0. It should be noted, however, that under operating conditions, the coupled interaction between structural deformation and the electric field leads to a more complex relationship between p_e, n, and V_0. Nevertheless, an overall increase in p_e with increasing n is clearly observed, as shown in Fig. 31.

Consistent with the observations in Section 5.4, variations in the electrostatic pressure induced by changes in n do not alter the dominant deformation mode of the tube. For $T_w = 1.5$ s, the tube deformation remains governed by the 2nd-order mode across the entire range of DEG layers considered, as illustrated in Fig. 32.

Although the deformation mode remains unchanged, the increased electrostatic pressure effectively “softens” the tube, leading to a pronounced increase in deformation amplitude. As shown in Fig. 33(a), when n increases from 1 to 6, the normalised deformation amplitude $A_S(x)/\overline{S}(x)$ at the mid-length section ($x/L = 0.5$) increases from 0.114 to 0.148, corresponding to an increase of approximately 29.8%. This enhanced deformation is accompanied by a corresponding rise in structural stress. As indicated in Fig. 33(b), the maximum von Mises stress on the tube surface increases from 1.253 MPa to 1.540 MPa over the same range of n, representing an increase of approximately 22.9%.

5.5.2. Electrical power generation

The number of DEG layers affects the electrical power output of the S3 WEC primarily by altering the capacitance variation of the embedded DEG units. Changes in capacitance also influence the voltage evolution within the control circuit, thereby indirectly affecting the power output.

Fig. 34(a) shows the temporal variation of the instantaneous electrical power P_t for different numbers of DEG layers. The variation amplitude of P_t increases markedly with increasing n. Specifically, when n increases from 1 to 6, the variation amplitude of P_t increases by approximately a factor of 35. The time-averaged electrical power $\overline{P}_t$ exhibits a similar trend, increasing rapidly with n, as shown in Fig. 34 (b). Over the same range, $\overline{P}_t$ increases from 0.0444 W to 1.96 W, corresponding to an increase by approximately a factor of 44.

Similarly, the number of DEG layers should be selected by balancing power enhancement against the associated increase in structural loading and output variability. For configurations with a larger number of DEG layers, local reinforcement or stiffness tailoring in critical regions may provide a practical route to improve structural survivability.

6. Conclusions

In this study, a high-fidelity multiphysics modelling framework was developed to investigate the coupled FSE response of the S3 flexible tube WEC equipped with distributed DEG units. The framework integrates computational fluid dynamics, finite element structural modelling, and a lumped electromechanical DEG model within a strongly coupled two-way solution strategy, thereby capturing the dynamic feedback among the three physical domains. The modelling approach was validated against experimental measurements of voltage-induced axial deformation of a cylindrical dielectric elastomer actuator and was then used to systematically examine how wave conditions and electrical parameters govern the coupled dynamic response and energy conversion performance of the S3 WEC.

The main conclusions of this study can be summarised as follows:

1. Electrostatic pressure has only a limited influence on the surrounding flow field, whereas its primary effects are manifested in the structural response of the flexible tube and resulting electrical output.
2. The electromechanical effect is strongly dependent on wave period. At short wave periods ($0.9 \text{ s} < T_w < 1.2$ s), electrostatic pressure modifies the effective tube stiffness and alters bulge wave propagation, leading to changes in the dominant deformation mode. At longer wave periods ($1.2 \text{ s} < T_w < 2.42$ s), the deformation mode remains unchanged, while the deformation amplitude increases significantly due to stiffness softening.
3. The observed stress response is governed by the competition between deformation-mode modification and deformation amplification. This explains the reduction in peak stress at intermediate wave periods ($0.9 \text{ s} < T_w < 1.7$ s) and the increase in

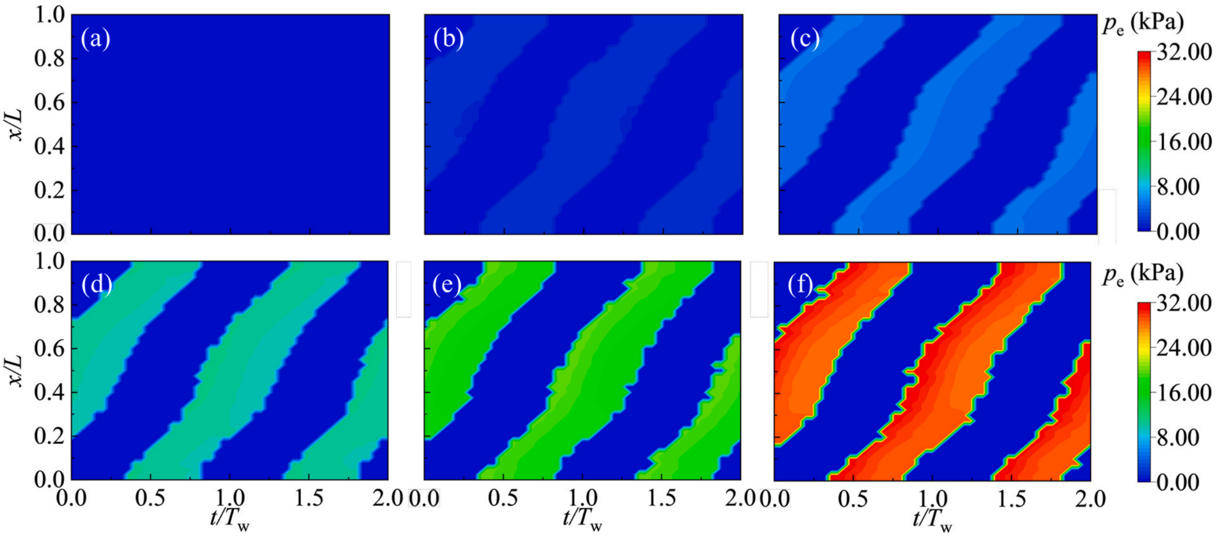

Fig. 31. Spatiotemporal distributions of the electrostatic pressure p_e acting on the tube surface for different numbers of DEG layers at $T_w = 1.5$ s: (a) $n = 1$; (b) $n = 2$; (c) $n = 3$; (d) $n = 4$; (e) $n = 5$; (f) $n = 6$.

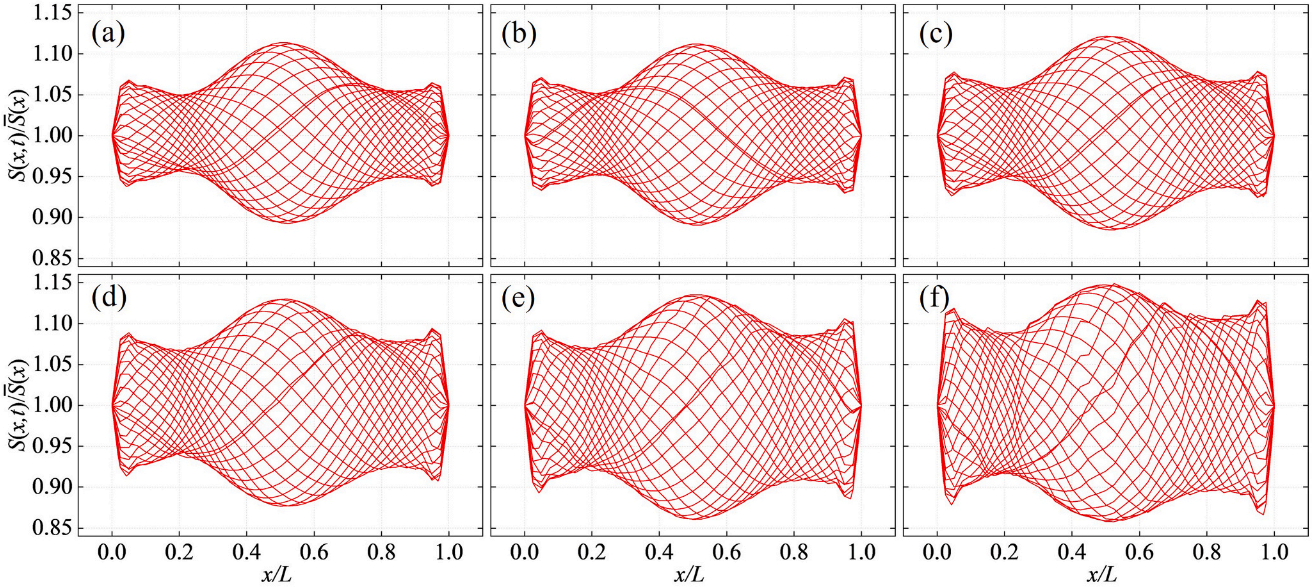

Fig. 32. Tube cross-sectional area $S(x,t)$, normalised by the time-averaged cross-sectional area $\overline{S}(x)$, at selected instants within one wave period for different numbers of DEG layers at $T_w = 1.5$ s: (a) $n = 1$; (b) $n = 2$; (c) $n = 3$; (d) $n = 4$; (e) $n = 5$; (f) $n = 6$.

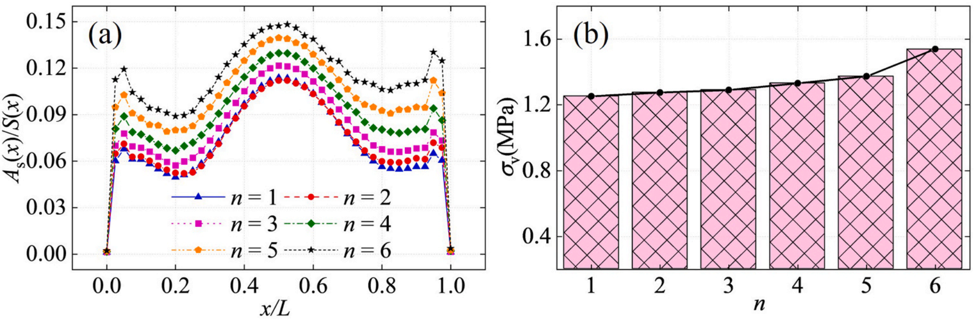

Fig. 33. (a) Deformation amplitude of the tube cross-sectional area, $A_S(x)/\overline{S}(x)$, under different numbers of DEG layers at $T_w = 1.5$ s; (b) Maximum von Mises stress σ_v on the tube as a function of the number of DEG layers n.

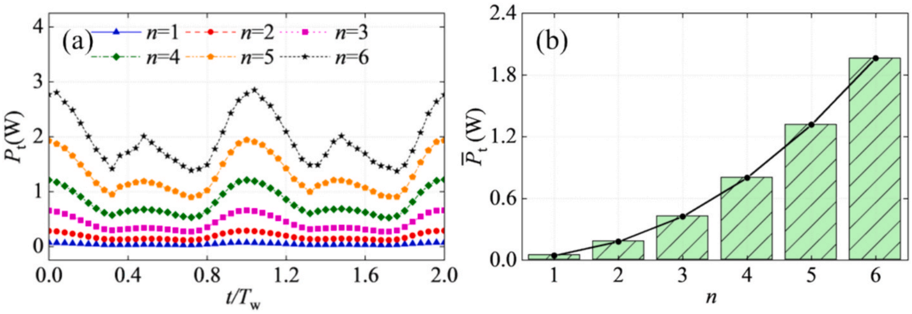

Fig. 34. Electrical power generation of the S3 WEC under different numbers of DEG layers at $T_w = 1.5$ s: (a) Instantaneous electrical power P_t; (b) Time-averaged electrical power $\overline{P}_t$.

stress at longer wave periods (1.7 s < T_w< 2.42 s), where deformation amplification becomes dominant.

(4) Larger deformation amplitudes lead to higher time-averaged electrical power output, but also to more pronounced temporal power variation and higher structural stress, highlighting a clear trade-off between enhanced energy capture and structural loading.

(5) Increasing incident wave amplitude intensifies fluid–structure interaction and enhances tube deformation. Although the dominant deformation mode remains unchanged, both the mean electrical power output and its temporal variability increase approximately linearly with wave amplitude.

(6) Electric-field-related parameters, including initial voltage and the number of DEG layers, primarily affect system performance by increasing electrostatic pressure and effectively softening the

tube. As a result, the deformation amplitude increases markedly, while both the time-averaged electrical power output and the amplitude of power variation exhibit an approximately quadratic dependence on the initial voltage and the number of DEG layers.

Overall, this work advances the understanding of FSE coupling mechanisms in flexible WECs and clarifies how wave and electrical parameters jointly govern deformation, stress, and electrical output. The results provide physically grounded guidance for the design and operation of DEG-integrated flexible tube WECs, particularly in balancing energy capture against structural loading and power variability. At the same time, the present study should be interpreted as a high-fidelity multiphysics modelling and mechanism analysis framework for early-stage assessment of DEG-integrated flexible tube WECs, rather than as a demonstration of immediate practical viability. The present framework still relies on simplified electrostatic modelling assumptions, which should be refined in future work. Further developments should also include more realistic material constitutive models and dedicated experimental validation of the fully coupled system under representative wave conditions.

CRediT authorship contribution statement

Yang Huang: Writing – review & editing, Writing – original draft, Visualization, Validation, Software, Methodology, Investigation, Formal analysis, Data curation, Conceptualization. **Qing Xiao:** Writing – review & editing, Supervision, Software, Resources, Project administration, Methodology, Funding acquisition, Conceptualization. **Liu Yang:** Writing – review & editing, Project administration, Funding acquisition, Conceptualization. **Saishuai Dai:** Writing – review & editing, Validation, Investigation, Conceptualization. **Saeid Lotfian:** Writing – review & editing, Conceptualization. **Feargal Brennan:** Funding acquisition, Conceptualization.

Declaration of competing interest

The authors declare that they have no known competing financial interests or personal relationships that could have appeared to influence the work reported in this paper.

Acknowledgements

This research was supported by an Engineering and Physical Sciences Research Council (EPSRC) Grant “Bionic Adaptive Stretchable Materials for WEC (BASM-WEC)” (EP/V040553/1). The authors gratefully acknowledge the support of the EPSRC High-End Computing Consortium for Wave Structure Interaction (HEC-WSI), under grant number EP/X035751/1, for providing access to ARCHER2 HPC resources.

Data availability

Data will be made available on request.

References

[1] Li H, Shi X, Kong W, et al. Advanced wave energy conversion technologies for sustainable and smart sea: a comprehensive review. Renew Energy 2025;238:121980.

[2] Arrosyid WA, Sari WR, Waskito KT, et al. Recent advancements in wave energy converter technologies: a comprehensive review on design and performance optimization. Ocean Eng 2025;340:122328.

[3] Guo C, Sheng W, De Silva DG, et al. A review of the levelized cost of wave energy based on a techno-economic model. Energies 2023;16(5):2144.

[4] Said HA, Sardá AC, Ringwood JV. Fault management in wave energy systems: diagnosis, prognosis, and fault-tolerant control. Ocean Eng 2025;316:119794.

[5] Bouhrim H, El Marjani A, Nechad R, et al. Ocean wave energy conversion: a review. J. Marine Sci. Eng. 2024;12(11):1922.

[6] Ahamed R, McKee K, Howard I. Advancements of wave energy converters based on power take off (PTO) systems: a review. Ocean Eng 2020;204:107248.

[7] Renzi E, Michele S, Zheng S, et al. Niche applications and flexible devices for wave energy conversion: a review. Energies 2021;14(20):6537.

[8] Collins I, Hossain M, Dettmer W, et al. Flexible membrane structures for wave energy harvesting: a review of the developments, materials and computational modelling approaches. Renew Sustain Energy Rev 2021;151:111478.

[9] Farley, F. J. M., & Rainey, R. C. T. (2011). U.S. Patent No. 7,980,071. Washington, DC: U.S. Patent and Trademark Office.

[10] Jean, P., Wates, A., Ardoise, G., Melis, C., Van Kessel, R., Fourmon, A., Barrabino, E., Heemskerk, J. & Queau, J. P. (2012, April). Standing wave tube electro active polymer wave energy converter. In Electroactive Polymer Actuators and Devices (EAPAD) 2012 (Vol. 8340, pp. 75-95). SPIE.

[11] Chaplin JR, Heller V, Farley FJM, Hearn GE, Rainey RCT. Laboratory testing the Anaconda. Philos Trans R Soc A Math Phys Eng Sci 2012;370(1959):403–24.

[12] A.C. Mendes, L.M.A. Paredes, F.A.S. Gil, J.R. Chaplin, Small-scale model tests of a rubber-tube wave energy converter with pneumatic power take-off. In International Conference on Offshore Mechanics and Arctic Engineering (Vol. 45530, p. V09AT09A029). American Society of Mechanical Engineers.

[13] A.C. Mendes, F.P. Braga, L.M.A. Paredes, J.R. Chaplin, 2017, June). Performance assessment of the ANACONDA WEC in regular waves at 1: 50 model scale. In International Conference on Offshore Mechanics and Arctic Engineering (Vol. 57786, p. V010T09A016). American Society of Mechanical Engineers.

[14] Yu H, Bai Z, Shi Y, Zhao C, Liu X, Wang Y. Hydrodynamic performance of an elastic capsule oscillating water column type WEC: an experimental study. Appl Ocean Res 2024;142:103850.

[15] Babarit A, Singh J, Mélis C, Wattez A, Jean P. A linear numerical model for analysing the hydroelastic response of a flexible electroactive wave energy converter. J Fluids Struct 2017;74:356–84.

[16] Zou S, Abdelkhalik O. A numerical simulation of a variable-shape buoy wave energy converter. J. Marine Sci. Eng. 2021;9(6):625.

[17] M.A. Shabara, Zou, S., & Abdelkhalik, O. (2021, June). Numerical investigation of a variable-shape buoy wave energy converter. In International conference on offshore mechanics and Arctic engineering (Vol. 85192, p. V009T09A013). American Society of Mechanical Engineers.

[18] Li X, Xiao Q. A numerical study on an oscillating water column wave energy converter with hyper-elastic material. Energies 2022;15(22):8345.

[19] Huang Y, Xiao Q, Idarraga G, et al. Bio-inspired adaptive flexible tube wave energy converters: resonant fluid–structure interaction and power extraction. Phys Fluids 2025;37(5).

[20] Huang Y, Idarraga G, Abad F, et al. Oscillating water column wave energy converter with flexible structured sheet material for enhanced power output. Energ Conver Manage 2025;333:119794.

[21] Huang Y, Xiao Q, Yang L, et al. Multiphysics analysis of a flexible oscillating water column wave energy converter with dielectric elastomer membrane. J Fluids Struct 2026;140:104447.

[22] Huang Y, Xiao Q, Idarraga G, et al. Novel computational fluid dynamics-finite element analysis solution for the study of flexible material wave energy converters. Phys Fluids 2023;35(8).

[23] Smagorinsky J. General circulation experiments with the primitive equations: I. the basic experiment. Mon Weather Rev 1963;91(3):99–164.

[24] Deardorff JW. A numerical study of three-dimensional turbulent channel flow at large Reynolds numbers. J Fluid Mech 1970;41(2):453–80.

[25] Christensen ED, Deigaard R. Large eddy simulation of breaking waves. Coast Eng 2001;42(1):53–86.

[26] Newmark NM. A method of computation for structural dynamics. J Eng Mech Div 1959;85(3):67–94.

[27] Yan FN, Wong HK. Force between the plates of a parallel-plate capacitor. Am J Phys 1993;61(12):1153.

[28] Jasak H, Jemcov A, Tukovic Z. OpenFOAM: A C++ library for complex physics simulations[C]//International workshop on coupled methods in numerical dynamics. 2007, 1000: 1-20.

[29] Dhondt G. Calculix crunchix user’s manual version 2.12. Munich, Germany, accessed Sept, 2017, 21: 2017.

[30] Degroote J, Bathe KJ, Vierendeels J. Performance of a new partitioned procedure versus a monolithic procedure in fluid–structure interaction. Comput Struct 2009;87(11–12):793–801.

[31] Lindner F, Mehl M, Uekermann B. Radial basis function interpolation for black-box multi-physics simulations. 2017.

[32] Carpi F, De Rossi D. Dielectric elastomer cylindrical actuators: electromechanical modelling and experimental evaluation. Mater Sci Eng C 2004;24(4):555–62.

[33] Moretti G, Rosati Papini GP, Daniele L, et al. Modelling and testing of a wave energy converter based on dielectric elastomer generators. Proc R Soc A 2019;475(2222):20180566.

[34] Higuera P, Lara JL, Losada IJ. Three-dimensional interaction of waves and porous coastal structures using OpenFOAM®. Part I: Formulation and validation. Coast Eng 2014;83:243–58.

[35] Higuera P, Lara JL, Losada IJ. Three-dimensional interaction of waves and porous coastal structures using OpenFOAM®. Part II: Application. Coast Eng 2014;83:259–70.